Probes for Noninvasive Biological Visualization and Biosensing of Cancer Cells

Sachin Kadian¹*, Shubhangi Shukla¹*, Roger J. Narayan^{1#}

¹ Department of Biomedical Engineering, University of North Carolina and North Carolina State University, 27599, Chapel Hill, USA
*equal first author
#corresponding author
*Corresponding author: rjnaraya@ad.unc.edu

Abstract

The early detection of tumors and precancerous conditions is vital for cancer diagnosis. Advances in fluorescence microscopic techniques and materials synthesis processes have revolutionized biomarker detection and image-guided cancer surveillance. In particular, novel materials-based diagnostic tools and innovative therapies have facilitated a precise understanding of biological processes at the molecular level. This critical review presents an overview of bioimaging probes, including functionalized chromophoric systems, non-functionalized chromophoric systems, and nanoscale biosensors. Technical challenges and future directions related to these approaches are considered.

Keywords: AIEgens, FRET, upconversion luminescence, biomarker, cancer diagnosis, biosensors

- I. Introduction
- II. Photophysical mechanisms of fluorescence bioimaging
 - A. Aggregation-induced emission (AIE)
 - B. Photoinduced electron transfer (PET)
 - C. Forster resonance electron transfer (FRET)
 - D. Up conversion luminescence (UCL)
- III. Nanoscale biosensing probes for cancer biomarker detection
 - A. Nanomaterial-based electrochemical probes
 - B. Nanomaterial-based optical probes
 - i. Fluorescence-based optical nanoprobes
 - ii. SPR-based optical nanoprobes
 - iii. SERS-based optical nanoprobes
- IV. Conclusions and future outlook

I. Introduction

A significant amount of research in recent decades has been focused on advances in the diagnosis and treatment of cancer.^{1,2} Such improvements have increased the survival rates of individuals with various types of cancer since the mid-20th century. ¹⁻⁴ However, only moderate success has been achieved in curing individuals diagnosed with cancer at advanced metastatic stages. The limitations in managing localized and malignant cancers can be overcome with better identification of site-specific tumors. The initial detection of cancer involves technologies related to cancer onset and progression. 1-8 Typically, cancer development starts with chromosomal rearrangements or mutations in DNA sequences.⁴⁻⁸ Events such as point mutations, sequence amplifications, and epigenetic modifications interrupt the phases of the normal cell cycle from G0 (gap 0) to M (mitotic cell division) via terminal differentiation through G1 (gap 1) and S (DNA synthesis) stages. This process occurs through the activation of oncogenes RAS and MYC. In normal cells, RAS signals the reversible phosphorvlation of MYC and effectively activates the translation machinery. In tumorigenesis, the unregulated phosphorylation of MYC causes its accumulation and promotes the release of cell cycle drivers (e.g., CDK and cyclins).³⁻⁸ This phenomenon leads to the unavailability of tumor suppressor genes (e.g., p53, APC, BRCA_{1/2}) and impacts natural cell division, DNA repair, cell activity, and apoptosis (programmed cell death). Reactive oxygen species (ROS), such as superoxide, peroxide radicals, and other oxidative products of various cellular metabolic pathways, can bring about an oncogenic activation process. 1-8 It has been observed that the inhibition of oxidative products could either hinder or escalate the potential of early-stage tumor development as different kinds of behavior occur from the pro-oncological stage to advanced invasive cancer. Therefore, the stage-specific differential expression of ROS can generate proximal signaling for cancer inception, proliferation, and invasion. Additionally, malignant growths express specific cell receptor proteins over a period of time, which can be detected by various bioimaging⁶⁻⁹ and biosensing^{7,10-11} approaches.

A number of live cell imaging techniques have been developed to obtain the required sensitivity and selectivity for early cancer diagnosis. 9,12-14 Among them, fluorescence microscopy (FM) facilitates the precise assessment of the physiological environment; in addition, it can distinguish between healthy and diseased cells at sub-cellular resolution. FM provides a window to sharper and faster imaging with superior contrast even with poor signaling from fluorophore molecules (e.g., at minimal availability of excitation light during photobleaching episodes). 12-14 Recently developed advanced procedures in FM (e.g., single molecule, light sheet, lattice light sheet fluorescence microscopies) deliver super-resolved visualization (~<30 nm) and exhibit significant potential for diffraction-limited resolution over large fields of view. 12-14 This kind of imaging is made possible by adding suitable fluorescence probes, which undergo specific photophysical mechanisms to locate the intended cellular region. Similarly, biosensing is another noninvasive and effective alternative for early cancer diagnosis. Many biosensors are based on the detection of cancer-related metabolites, which are obtained

from various circulating body fluids. Among all of the broadly employed approaches in cancer research, nanomaterials-based biosensors have led to various encouraging outcomes for cancer diagnosis. Nanoscale materials are often used for electrode surface alteration, catalysis in reactions, signal amplification, and molecular labeling; several reports have indicated that nanoscale materials enhance the sensitivity of biosensing platforms due to their large-area-to-volume ratio values. Moreover, nanoscale materials increase the electron transfer capability of electrodes, enhance the attachment of biological elements to the sensing platform, and reduce the sensing time. These nanostructured electrodes convert the biological activity exhibited by the interaction between biorecognition molecules and target biomarkers into measurable electrical or optical signals. Depending on sensing probes used to convert these signals, the cancer biomarker detection approaches are designated either as electrochemical or optical biosensors. This review focuses on promising bioimaging and biosensing processes for cancer detection.

II. Photophysical mechanisms of fluorescence bioimaging

Bioimaging techniques for cancer diagnosis have evolved over several decades. Various efforts involving radioisotopic imaging, X-ray imaging, tomography, ultrasound, resonance imaging, cellular mapping, and molecular mapping with emerging optical imaging techniques have been described. 12-13 Optical imaging depends on the pattern of light interaction with the matter, which can be transmission, reflection, or fluorescence. 12 Among these approaches, the use of fluorescence for cancer cell imaging has evolved since the 1920s, when porphyrin was used as an imaging probe for tumors. 12-15,18-20 The use of fluorescein to visualize brain tumors was demonstrated in the 1940s. A super-resolved form of fluorescence microscopy known as stimulated emission depletion (STED) was developed in the 1990s.^{21,22} This approach generated differentially resolved images by focused illumination and region-specific fluorescence emission. The STED process interrupts the traditional fluorescence at the photon release stage by forcing the electron to relax at a higher vibrational energy state instead of the usual S₀ state, leading to emission at far-red wavelengths. This approach can enable cellular imaging at a lower optical diffraction limit of < 50 nm. ^{21,22} However, the selective deactivation of fluorophore emission requires a high intensity of photons, which leads to the thermal destruction of biological systems and the photobleaching of small organic molecule-based fluorescence probes.²⁰⁻²⁴ Moreover, to facilitate molecular-level analysis of disease, images need to be temporally resolved and sensitive to molecular agitations in the biological environment; moreover, the probes involved should be photostable, biocompatible, and compatible with dynamic imaging. 12-15,18-24 The fluorescence phenomenon imparts contrast to images; as such, it can be used to discriminate between relevant and backdrop features. Also, it provides the capability for real-time monitoring of dynamic physiological events in normal and diseased environments. 12-15,18-24 This selectivity of fluorescence emission has enabled image-guided detection of malignancies and is the backbone of continuously evolving fluorescence microscopic techniques. Confocal laser scanning microscopy (CLSM) has enabled three-dimensional imaging and imaging of deep tissues.^{23,24} Hence, fluorescence imaging has transformed the in vivo evaluation of cancer growth and depth due to its capacity to assess the tumor proliferation stage. Sensitive

fluorescence imaging probes can help evaluate metastasis and cancer cell invasion as well as assess image-guided therapy. ^{12-15,18-29} Cancer stem cells at infected sites overexpress certain cancer-specific proteins, enzymes, and cell receptors. ^{14,18-22} As such, the fluorescent probes can be conjugated with biomarkers, which can bind recognition factors at tumor sites. ^{14,18-24} A class of several luminogens or fluorophores with an enhanced fluorescence signal after reaction with the target biomolecule has been developed for cancer detection and diagnosis. ^{14,18-27}Additionally, issues such as endogenous tissue autofluorescence, low scattering from hemoglobin, low-depth imaging, and wavelength-related cytotoxicity can be mitigated by low-frequency irradiation with near-infrared photons, which cover the entire therapeutic window (700 – 1000 nm). ^{26,27} Materials such as fluorescent carbon dots, quantum dots, lanthanide ion-doped nanomaterials, organic fluorophores, polymeric fluorescent nanoparticles, photo-luminescent silicon nanoparticles, and chromophore-modified metallic nanoclusters have been used for this purpose. ²⁵⁻²⁷ These probes undergo radiative emission by mechanisms such as the following:

- 1. The aggregation-induced emission (AIE) effect involves "turned-on" fluorescence in the aggregated state, which ensures greater resistance to chemical and photodegradation.^{28,29} As such, AIE luminogens can withstand light irradiation for an extended duration; as such, these materials are useful for cancer cell imaging. Most AIEgens are biocompatible, exhibit a high cellular uptake, do not stimulate pathological changes, and do not cause inflammation in the nearby healthy tissue.³⁰⁻⁴⁵
- 2. The photoinduced electron transfer (PET) effect involves an "off–on" mode sequence of fluorescence. 46-60 In a PET probe acceptor-donor duo, fragments may exist intramolecularly; alternately, receptor and fluorophore centers are in proximity to a short spacer. 46-60 According to the direction of electron flow, the PET process is categorized as a PET and d PET. Once the receptor end binds with the targeted biomarker, fluorescence turns "on," and PET is restricted. 46-60 This mode of fluorescence is actively operated as compared to passive conventional photon emission. This approach is useful for bioimaging as it creates spatially resolved images of living cells. 46-60 This mode of fluorescence is actively operated as compared to passive conventional photon emission. This approach is useful for bioimaging as it creates spatially resolved images of living cells. 46-60 This mode of fluorescence is actively operated as compared to passive conventional photon emission. This approach is useful for bioimaging as it creates spatially resolved images of living cells.
- 3. The Forster resonance electron transfer (FRET) effect is a ratiometric fluorescence strategy, in which high-frequency photon emission of the donor segment facilitates low-frequency or red–shifted emission of the acceptor nucleus. 61-71 As a process for bioimaging, FRET enables an understanding of disrupted protein–protein interactions associated with the cancer cell microenvironment, the efficiency anticancer therapeutics, and the dynamics of tumor growth via live cell imaging; moreover, FRET allows for the evaluation of aberrations in kinase activity associated with abnormal cell proliferation, downstream signaling pathways by specific ligand-receptor interactions on the cell surface, and conformational changes in transmembrane proteins responsible for regulating ion channels, .72-78 Further, this specialized approach is often combined with fluorescence lifetime imaging microscopy (FLIM), which can detect changes in

luminophore structure with respect to temperature, pH, and molecular forces in the cellular environment, regardless of the probe concentration.⁷⁹⁻⁸¹

FRET prevents the photobleaching of a fluorophore probe depending on the presence and absence of an acceptor at a threshold distance from the donor and the resonant energy transfer between two emissive nuclei. Therefore, FRET efficiency is related to photobleaching by the following equation:

$$E = 1 - \frac{t_{pb}}{t_{pb}} \tag{1}$$

In this equation, t'_{pb} and t_{pb} represent the photobleaching decay time constant values of the donor in the absence of the acceptor and the presence of the acceptor, respectively. In upconversion luminescence, anti-Stokes emission depends on elemental doping in a nanoscale matrix. Single wavelength excitation can result in differential-shade imaging along with enhanced buildup at intended tumor sites than around normal tissues due to an enhanced permeability and retention effect.⁸²⁻¹⁰⁰ The following sections describe these photophysical mechanisms underlying the effective in vivo fluorescence imaging of cancer cells.⁸²⁻¹⁰⁰

A. Aggregation Induced Emission

The photophysical phenomenon through which weakly fluorescing molecules in solutions undergo bright fluorescence on aggregation is termed aggregation-induced emission (AIE). This technological evolution offers an interesting platform to visualize molecular-level structure-property relationships.³⁰⁻³⁹ The AIE effect can induce light emission in the solid-state, which is of practical importance in OLED and other applications. In the 1920s, it was observed that some luminogens could fluoresce well in highly viscous solutions or the aggregated state compared to dilute systems.³⁰ In the 1960s, a relationship between internal molecular rotations and light emission was established.³⁰ The non-planar polyaromatic, bulky luminogens with propeller-like structures (e.g., silole, Fig. 1A (1-3)) were found to be emissive at higher concentrations as compared to the planar ones (e.g., pyrene) which undergo non- emissive fluorescence (quenching) due to $\pi - \pi$ stacking in similar conditions (known as aggregated quenching effect (ACQ)). ³⁰⁻³⁵ Moreover, AIE luminogens such as silole, triphenylmethane derivatives, and stilbenes [Fig. 1A-3] show diminished fluorescence in dilute systems because of rapid intramolecular rotations, which interfere with the fluorescence lifetime of a molecule; these conformational changes are restricted on aggregation, resulting in intense fluorescence. 30-36 Recently, it was noted that the AIE effect originates from delimited intramolecular rotational and vibrational motions (termed RIR / RVR) in the molecule under aggregated conditions. 30-33 RIR is the rational mechanism that utilizes the functional AIE effect in AIE luminogens or solid-state emitters. Different categories of AIE luminogens include hydrocarbon, heterocyclic, supramolecular, polymeric, and organometallic materials. 30-39 Luminogenic molecules that have multiple aromatic rings connected to the single conjugated centers such as fulvenes, polyarylated ethenes, pyrans, butadienes, and arylenes show the AIE effect with emission in the visible spectrum.

Taking the example of the first AIEgen, hexaphenylsilole (HPS) stays non-luminescent in dilute solutions due to a dynamic rotational state and promotes non-radiative annihilation from the excited state [Fig. 1A-2]. On aggregation, it undergoes radiative emission due to RIR, which blocks the non-radiative channel. The RIR mechanism was tested on HPS under different conditions; it was observed that the viscosity of the medium served as a reverse drag on intramolecular rotations and proportionately improved the emission. Moreover, pressurization or pleochroism in liquid as well as in solid systems shortened the distance between molecules. It filled the void volume, thereby restricting the intramolecular rotations, leading to excimer formation and enhanced emission. In addition, structural rigidification in a freely rotating twisted molecule (HPS) through substitution at specific positions can restrict the internal rotations even in dilute systems, leading to bright fluorescence emission. 30 Taking advantage of these unique properties, AIEgens are considered to be excellent exogenous contrast materials for fluorescence imaging.³⁰⁻³⁹ Upon bonding with biomarkers or incorporation in a biological system, the surrounding biological environment restricts the intramolecular motion in loose AIE molecules, and the bright emission from AIEgens can therefore be used to detect tumor sites or malignancies.³⁵⁻³⁸ AIEgens are tolerant to photobleaching upon laser exposure; as such, they can facilitate long-lasting tracing of dynamic biological processes such as cancer growth and proliferation. 30-45 AIEgens with low levels of cytotoxicity have gained attention for imaging the intracellular environment and tracking various cellular processes. 40-44 For instance, an AIEgen biological probe of tetraphenylsilole (TPS) conjugated with cyclic Arg-Gly-Asp (cRGD) and Asp-Glu-Val-Asp (Ac-DEVD) peptide sequences was able to effectively target the integrin avb3 receptor expressed by U87MG human glioblastoma cancer cells. 41 Several groups have synthesized similar phosphorescent derivative molecules with the AIE effect for cancer cell bioimaging applications under ambient conditions.

In a study, Tan et al. prepared a dual-mode AIEgen probe for lipid droplet (LDs) that may be useful for in vivo imaging and intracellular photodynamic therapy (PDT). 42 LDs organelles that are variable in nature; these structures exhibit changes due to variations in the cellular environment. These structures deal with the metabolism of important biomolecule signal transduction and membrane transport. 42 The aberrations in LDs of cells serve as biomarkers for various diseases, including cancer growth. The group used a biheteroaryl core bridged AIEgen with red/near infrared emission. Bridging with the biheteroaryl subunit contributed to the extension of π -conjugation in the whole molecule, as shown in Fig. 1B-1. 42 The bioimaging probe was obtained over several steps of chemical reactions: (a) bromination at the imidazole core in 2-furylated imidazole to give 5-bromo-2-furylated imidazole, and (b) this structure undergoes Suzuki Miyaura coupling with 4-(diphenylamino)phenylboronic acid and condensation reaction with malononitrile to give the required molecule TIFMN. 42 This AIEgen was used for cell imaging by introduction into 786-O cells and primary clear cell renal cell carcinoma (ccRCC) tumor cells. 42 The confocal images of TIFMN stained LDs in 786-O cells (shown in Fig. 1B-2 at different times) clearly track

the highly resolved spatial distribution of LDs in these living cells. The LDs-related bioimaging in AIEgen tumor cells showed high spatial and temporal resolution with bright red fluorescence emission.⁴²

Long et al. investigated the role of mangiferin, a water-soluble luminogen with medicinal and bioimaging properties.⁴³ It is a natural AIEgen containing a C-glucoside group, which shows a significant Stokes shift (λ=165 nm) [Fig. 1C-1].⁴³⁻⁴⁵ The fluorescence spectra of mangiferin showed a strong emission around 420 nm with an increase in molar concentration; another emission peak at 545 nm is strongly enhanced.⁴³ The two emissions were indexed to monomer and static excimer formation; the latter has a large Stokes shift from the absorption spectra.⁴³ The excimer emission at 545 nm corresponds to the bioimaging window.⁴⁴ Being a natural product of mango leaves, it shows biological activity by binding with specific receptors in the cellular environment. Mangiferin can recognize targeted factors without additional functionalization using biomarkers.⁴³ They observed that a mitochondrial membrane protein, known as B-cell lymphoma 2 (Bcl-2), could specifically bind with mangiferin via the C-glucoside group.⁴³ Owing to this specific interaction, mangiferin was injected intravenously into a tumor-bearing mouse. Fluorescence microscopic images showed the complete distribution of the material over the course of 30 min. After an hour or so, the fluorescence intensity increased in tumor tissues, indicating the accumulation of mangiferin in cancer cells. In contrast, healthy cells did not show any enhancement.⁴³ Thus, the imaging interpretation confirmed mangiferin interaction with cancer cells. In addition, the cytotoxicity of mangiferin was investigated in different cancer cells (SW480, MCF-7, HeLa, and SKOV-3) and corresponding healthy cells (e.g., NCM460, MCF-10A, H8, and IOSE80). Fig. 1C-2 shows that normal cells maintained higher cell viability rates than cancer cells.⁴³

Hu et al. reported on the development of AIEgen, which can be used for cancer cell bioimaging along with noninvasive cancer therapy and PDT in a simultaneous manner. ¹⁰¹ They used tetraphenyl ethylene (TPE) as core nuclei to obtain a red emissive luminogen since it exhibits an abnormal aggregation-induced emission (AIE) behavior. TPE was further functionalized; in particular, it was chemically modified with electron-withdrawing and donating groups to induce a red shift in emission and provide a red emissive AIE luminogen. A cyano group containing electron-attracting moiety (- PhC = C (CN)2) was added as a photosensitizer for the PDT process in order to generate reactive oxygen species (1 O₂). ¹⁰¹ In addition, TPE-red was incorporated with a peptide sequence AP2H (IHGHHIISVG), which can specifically bind with a hydrophilic extracellular loop (EL2,PYRDDVMSVN, MW 1194.5) that is associated with a tumor-related protein called lysosomal protein transmembrane 4 beta (LAPTM4B). Thus, the complete assembly of AIEgen formed (TPE-red-2AP2H), which was noted to behave as a high contrast agent for bioimaging in cancer cells. The specific binding activity of TPE-red-2AP2H with LAPTM4B protein was traced for fluorescence imaging. The probe was found to exhibit excellent penetrability into the cells owing to LAPTM4 B-led transportation as compared to normal cells. Additionally, singlet oxygen species were released into tumor

cells on activation of the photosensitizer molecule; this mechanism can provide theranostic functionality for interaction with cancer cells.¹⁰¹

Tang et al. described a trifunctional luminogen system for several simultaneous activities, including gene therapy, fluorescence bioimaging, and cancer growth (PDT) treatment.¹⁰² They developed a two–photon (TP), near-infrared (NIR), and aggregation-induced emission (AIE) fluorescence probe, which exhibited a low rate of autofluorescence, high depth penetration, strong photosensitization (e.g., production of reactive oxygen species (ROS)), which supported the spatially resolved fluorescence imaging and PDT functionalities. The triphenylamine derivatives were chemically modified in two sequential steps with aneN3 and large hydrophobic hydrocarbon chains to provide TP NIR AIE characteristic features. The structure can provide ROS generation, strong NIR emission around 550 – 870 nm, highly resolved imaging of living cells, and TE gene expression.¹⁰²

B. Photoinduced Electron Transfer

The transfer of an electron to or from an electronically excited state of a molecule upon irradiation is referred to as photoinduced electron transfer (PET). 46-52 Either the excited molecule gets reduced or oxidized; in other words, it can undergo acceptor – excited (a-) PET/donor – excited (d-) PET processes. This phenomenon can be represented in the form of the equations as follows:

$$M + I \rightarrow M^* + Q \rightarrow M^{\circ +} + Q^{\circ -}$$
 (2)

$$M + I \rightarrow M^* + Q \rightarrow M^{\circ -} + Q^{\circ +} \tag{3}$$

In these equations, M is a molecule (donor/acceptor) undergoing excitation upon irradiation (I) to give M* (excited 'M'); Q is another molecule in the vicinity, which can take part in oxidation or reduction processes. A process similar to a photovoltaic cell, in which hole or electron generation and migration occur for electric field production, is envisaged. In this case, light excitation or photon absorption triggers the oxidative or reductive quenching by lowering the energy of the reductive hole in LUMO and increasing the energy of the oxidative electron in HOMO of the ground state of the molecule. A for instance, diamino fluoresceins (DAF) obtained by amino group substitution at the benzene moiety of fluorescein nucleus do not show fluorescence emission. This phenomenon is attributed to electron donation from the benzene nucleus to the electron-deficient acceptor xanthene nucleus, which coincides with the a – PET phenomenon. Interaction with some molecules and conversion of benzene to the imidazole moiety by ring closure lead to the generation of the fluoresceing molecule (DAF-T). The HOMO of the benzene donor has higher energy than the acceptor HOMO; after the acceptor molecule is excited, the electron from the donor HOMO is transferred to the acceptor HOMO due to a – PET process. This phenomenon creates cationic and anionic radicals [Fig. 2A].

can be regulated by a-PET from the benzene moiety to the acceptor fluorophore.⁴⁹ On the other hand, by activating the d-PET process, the fluorescence behavior of a derived molecule can be reversibly controlled [Fig. 2B]. By substituting the benzene moiety with electron-withdrawing groups, the structure becomes rather electron deficient in comparison to the xanthene moiety in fluorescein; as such, the flow of electrons will be directed from xanthene to the benzene nucleus.⁴⁹ This situation is where d – PET comes into the picture; on excitation of the donor electron to LUMO, the electron from the acceptor HOMO is transferred to the donor HOMO, and the fluorescence is quenched.⁴⁹ As such, the fluorophore derivatives undergo quenching because of intramolecular electron transfer either via a – PET or d – PET pathways and can show emissive behavior in the presence of specific molecules (e.g., DAF shows fluorescence on reaction with nitric oxide (NO)).⁴⁷⁻⁴⁹ Similarly, other fluorophore derivatives fluoresce brightly in the presence of ROS, HOCl, pH changes, specific peptide sequences, or specific ions (Zn²⁺).⁴⁹⁻⁵⁵ Since these molecules or metabolites are expressed by cancer-affected tissues, the PET mechanism can be utilized for optical imaging of tumor sites by combining with these specific cell receptors.^{55-60,103-105} Typically, PET probes demonstrate an unconventional type of fluorescence mode (i.e., "off-on"), which is widely used for designing cancer cell bioimaging tools.^{52-60,103-109} Recent findings involve bioimaging of cancer cell activity via PET interaction with expressed factors such as metal ions like Zn²⁺ [Fig. 2A-H], alterations in the physiological environment (e.g., intercellular pH, reactive biological species, and temperature), and the presence of cancer-specific enzymes (e.g., KIAA1363, COX-2, and Pim-1).^{50-60,103-109}

Huang et al. created a dual-mode bioimaging assay based on photoinduced electron transfer (PET) and a hyperchromic effect with polyethyleneimine-capped copper nanoclusters (PEI-Cu NCs). They investigated the detection and bioimaging of alkaline phosphatase (ALP) in the human lung adenocarcinoma cell line (A549 cells) through its catalytic conversion to p-nitrophenol (PNP) in the presence of p-nitrophenyl phosphate (PNPP). The hydrogen bonding interaction of the nanoclusters and in situ-generated p-nitrophenol effectively quenched the fluorescence of the PEI-CuNCs probe due to PET. In addition, the electron delocalization between polyethyleneimine and PNP led to strong ultraviolet absorption because of the hyperchromic effect [Fig. 2H]. Bioimaging in A549 cells was performed by culturing these cells with PEI-Cu NCs in the absence or presence of 10 mM PNPP [Fig. 2E]. A549 cells with nanoclusters gave a bright blue-green fluorescence; this phenomenon indicated the internalization of the material. While in the presence of PNPP, the fluorescence intensity was decreased due to the hydrolysis of PNPP by endogenous ALP in the cells. These results indicated the feasibility of a dual-mode system for efficiently monitoring intracellular ALP levels in cancer cells.

Sun et al. designed several types of probes for cyclooxygenase-2 (COX- 2) dependent cancer diagnosis in living cells involving PET.¹⁰⁷ They developed a fluorescent probe (ANQ-IMC-6) for COX- 2 driven fluorescence by combining indomethacin (IMC, an inhibitor of COX-2) and a fluorophore named acenaptho[1,2-b] quinoxaline (ANQ).ANQ-IMC-6 interacted with COX-2 upon cell internalization; a characteristic fluorescence was observed due to this interaction.¹⁰⁷ Later, an unfolding of its conformation led to an intense fluorescence

signal and turned off the PET phenomenon. Another probe system was developed based on a similar folding concept, involving a COX – 2 dependent two-photon probe called BTDAN-COX-2. This material can potentially detect ultratrace levels of COX-2 in cancer cells more selectively than ANQ-IMC-6. Another COX – 2 probe (Niblue-C6-IMC, or NANQ-IMC6) was prepared from the combination of Nile blue and a hexanediamine linker. ¹⁰⁷ Niblue-C6-IMC was successfully internalized into the tumor cells of a mouse. Depending on the PET folding mechanism related to the COX-2-specific interaction, this probe could differentiate cancer cells and normal cells via the strong fluorescence emission at ~ 615 nm. Another study described a PET-based fluorescence probe for diagnosing breast cancer. The cancer is expressed by an enzyme called cholesteryl ester hydrolase 1, (KIAA1363). They reported the formulation of fluorescence turn-off and on features in the system with a fluorophore (NB) and the inhibitor (AX) combination, which specifically targeted the enzyme KIAA1363 (as shown in Fig. 2D). ¹⁰⁷ Its interaction with probe NB-AX could efficiently and rapidly detect breast cancer cells via flow cytometry as well as image the unaffected tissues surrounding the breast tumor cells. ¹⁰⁷

Du et al. investigated bioimaging of cancer in the human prostate using AND logic-based fluorescence probes. ¹⁰⁸ This molecular logic function resembles a system that can simultaneously detect the two bioanalytes. They developed several fluorescent probes (referred to as DPP-C2, LysoDPP-C3, and LysoDPP-C4), which contained a diketopyrrolopyrrole (DPP) moiety to detect acidic pH values and the concentration of Zn²⁺ions in the lysosomal environment. Zn²⁺ is responsible for inhibiting the m-aconitase enzyme activity and thereby controls the production of citrate in the prostate fluid for normal prostate function. In prostrate cancer, the levels of Zn²⁺ varied more widely as compared to healthy conditions. This phenomenon is used as a biomarker for the differentiation of prostate cancer cells from healthy tissues. In addition, the lysosomal organelles exhibit an acidic environment. As such, the lysosomal acidic pH and Zn²⁺ ion concentration in prostate cells were used to develop a PET-based fluorescent probe. ¹⁰⁸ At low pH values and chelation of Zn²⁺ with the fluorophore, the fluorescence intensity increased after the PET pathway was blocked, as shown in the mechanistic pathway (Fig. 2C). LysoDPP-C4 probe was internalized in two prostate cancer cell lines (e.g., DU145 and PC3 cells) and normal RWPE human prostate cells. Almost negligible cytotoxicity for the probe was noted in cancer cells. The increase in the concentration of Zn²⁺ in RWPE1 cells led to an increase in fluorescence intensity when compared to cancer cell lines, which did not show a considerable change [Fig. 2F]. This behavior in cancer cells was attributed to the reduction in zinc transporters in DU145 and PC3 cancer cells, which do not enable the exchange of extracellular Zn²⁺. ¹⁰⁸

Chen et al. prepared a fluorescent probe for recognizing high levels of COX – 2 in cancer cells.¹⁰⁹ They used COX – 2 inhibiting fluorophores (e.g., indomethacin) along with coumarin, which were connected via different linkers. The two fluorophores quench the fluorescence of each other via donor-excited PET. The indomethacin inhibited coumarin fluorescence to give absorption and emission at higher wavelengths. ADC-6 and ADC-2 were the reference compounds; ADC-IMC-6 and ADC-IMC-2 were indomethacin-containing

probes [Fig. 2G]. The interaction of all of the probes with the COX-2 enzyme was analyzed. For ADC-IMC-6 and ADC-IMC-2, blue-shifts in the emission maxima were obtained on the addition of COX – 2 doses without any considerable changes in intensity; no changes were observed for the reference compounds ADC-2 and ADC-6. This finding was attributed to the high affinity of COX – 2 for indomethacin molecules. ADC-IMC-6 and ADC-IMC-2 probes were found to exhibit selective behavior for human serum albumin (HSA) protein over BSA; a great enhancement in the fluorescence intensities of the materials was observed. This selective relationship of indomethacin probes was tied to HSA and anticancer drug delivery; differentiation of cancer tissues from nearby healthy tissues was obtained.

C. Forster resonance energy transfer (FRET)

FRET is a through space phenomenon of radiation-less energy transfer, which takes place between a donor and an acceptor fluorophore nucleus. The efficient energy transfer is noted to depend on the distance of relative association (1 – 10 nm) between the FRET pair. 61-65 The fluorescence of the donor molecule decreases with the subsequent increase in acceptor fluorescence or non-fluorescence, which is observed depending on the properties of the involved molecule. 61-71,110-119 The concept was first coined by Jean Perrin in the 1920s as energy transfer between oscillating dipoles within the non-radiating near field space. This phenomenon was explained in 1948 by Theodor Forster as a radiation-less photophysical phenomenon that occurred between the energized fluorophore and the lower energy fluorescing molecule (acceptor) lying within a certain distance via dipole—dipole interactions. 61-63 The famous Jablonski diagram puts it as excitation/emission process between donor/acceptor fluorophores. According to IUPAC, the FRET phenomenon is also referred to as fluorescence resonance energy transfer. The FRET mechanism involves two steps: excitation of the donor from the ground state by photon absorption and energy transfer to acceptor nuclei. 61-71,110-118 The efficiency of the FRET process is described by the following equation:

$$E_{FRET} = \frac{R_0^6}{R_0^6 + R^6} \tag{4}$$

In this equation, R is the distance between two molecules. As evident from the above equation, the FRET efficiency is inversely related to R. Other than the distance, E_{FRET} is also controlled by other factors such as: a) the typical spectral overlap associated with the emission spectrum and the absorption spectrum of the donor and the acceptor, and b) dipole—dipole interaction, in particular a mutual orientation between the acceptor absorption and donor emission dipole moments.⁶¹⁻⁶⁴ The parallel alignment could generate a higher FRET efficiency than the perpendicular configuration. Several studies have emphasized adjusting the spectral overlap by modifying the molar absorption coefficient characteristics of the involved moieties.⁶¹ This process has been performed by chemical modifications in the molecules via ring closure or opening to generate fluorophores with various features that are responsible for the bioimaging functionality.^{65-71,110-119} The function of ratiometric-based fluorescence probes is almost independent of concentration, environment, and

excitation energy as compared to intensity-based ones.⁶¹⁻⁷⁰ These probes operate via the FRET phenomenon and are used for the development of nucleic acid, protein, as well as small molecule-based probes.^{65-71,110-119} These materials possess high selectivity and sensitivity toward the interference of molecules in their vicinity. The accuracy of FRET functioning and resolved bioimaging depends on the FRET pair selection and their specific placement in the surrounding environment [Fig. 3A].^{71,110-119} FRET is measured by several methods, including a) donor fluorescence, which can be described in terms of the fluorescence lifetime of the donor excited state in the presence or after bleaching of acceptor molecules, b) acceptor fluorescence, which involves a three cube approach to obtain different images on emission and is utilized for three-dimensional FRET imaging in cancer cells, spectral imaging, which measures the FRET efficiency and determines the accumulation or abundance of donor as well as acceptor molecules, and (d) fluorescence anisotropy, which is the degree of alignment between donor and acceptor dipole moments.⁶¹⁻⁷⁰ FRET duo elements can fall under intrinsic and extrinsic categories. The former ones are excited by high frequency radiation (e.g., UV-Vis radiation), which is undesirable in biological settings; the latter ones mostly involve polyaromatic nuclei, which imply low-energy NIR radiation and show effortless cellular uptake.^{61-71,110-119}

Kulkarni and Jayakanan investigated cancer cell imaging based on the photophysical FRET phenomenon. He had esigned a polymeric FRET probe using a biodegradable polycaprolactone triblock copolymer as backbone, which was attached with an assembly of π -conjugated block copolymer (oligo-phenylenevinylene (OPV)) in luminescence nanoparticles and served as a FRET donor molecule; Nile Red (NR) molecules served as a FRET antenna (acceptor). The FRET probe was determined to be biocompatible from cytotoxicity studies that were performed with various cancer cells (e.g., MCF 7, HeLa, and WT-MEF cells). This geometry could potentially restrict the donor–acceptor ends in proximity and inside the range of the Forster distance (20 – 60 Å). In fact, the FRET phenomenon was observed via confocal imaging in cancer cells. The fluorescence-tagged polycaprolactone block copolymer nanoparticle P30 (with monomer to initiator ratio = 30) displayed an emission from NR at ~ 595 nm before the photophysical FRET reaction, with an effective overlap of the emission spectrum and the absorption spectrum of the donor and acceptor. The first singlet excited state (LUMO) of NR (acceptor) was noted to be considerably above (-3.56 eV) that of the donor OPV molecule (-2.60 eV), which supported the energy transfer phenomenon. Moreover, time-correlated single photon count (TCSPC) studies demonstrated that the energy transfer (FRET) through a decrease in the average fluorescence lifetime value in the presence of the acceptor molecule (NR) in the probe. The laser scanning microscopy showed contrast images, with bright blue luminescence that was attributed to OPV self-emission as well as bright red luminescence in the NR range, which was followed by a FRET process that took place between the OPV and NR range [Fig. 3B]. Further, these results supported the suitability of this probe for dual imaging in cancer cells.

In another study, Zhang et al. investigated the fluorescence imaging of important endogenous metabolites, glutathione (GSH) and sulfur dioxide (SO₂), in tumor cells through an integrated FRET and intramolecular charge transfer (ICT) phenomenon [Fig. 3C].¹¹⁷ This scheme provides for reversible and rapid detection of GSH and SO₂ concurrently. Cyanoacetic acid functionalized coumarin (Mito-CM) and the CM treated with GSH (Mito-CM-GSH), both with a CN electron withdrawing group, were taken as donor nuclei for FRET-I and FRET-II systems [Fig. 3Ci-ii].¹¹⁷ Benzopyrylium unit (BP) was taken as acceptor nuclei in both due to significant spectral overlap of the CM-GSH and CM emission spectra with the BP absorption spectrum. In addition, the material contained exceptional interaction sites for SO₂. As such, the Mito-CM-BP probe showed responsive sites for SO₂ and GSH to facilitate a reversible photophysical phenomenon. In the presence of SO₂ to Mito-CM-BP moiety, the FRET-I process associated with Mito-CM-BP was quenched and the fluorescence emission associated with the CM moiety was restored with a working ICT reaction. Due to the presence of GSH in the surroundings, the π -conjunction between coumarin and cyanoacetic acid was suppressed; thus, the inhibited ICT process triggered the FRET-II process to the BP acceptor from the CM-GSH donor, which led to the amplification in emission radiation in the red portion of the visible spectrum. The addition of SO₂ at this instant destroyed the electron delocalization of BP nuclei; it resulted in the prevention of the FRET-II process as well as the release of donor emission (CMGSH). Therefore, the Mito-CM-BP combination of the FRET-ICT probe could successfully visualize the dysfunctional catabolic and anabolic GSH to SO₂ processes within tumor cells; thus, the energy transfer process could facilitate in vivo cancer imaging.¹¹⁷

Bahari et al. investigated the imaging of an oncogenic biomarker called MicroRNA-21 (miR-21) in cancer cells via the FRET technique. Its Fluorometric titration could more successfully quantify the indistinct and minute microRNA structures as compared to other analytical methods. The system exploited the property of enhancement in energy transfer with a greater spectral overlap of donor and acceptor centers in the FRET probe. Its The approach involved graphene (GQDs) and graphdiyene quantum dots (GDQDs) as an acceptor and a donor duo as a probe; these materials possess unique properties such as low cytotoxicity, high photostability, narrow spectral bandwidth, and high photoluminescence. Its GDQDs were tagged with DNA fragments, which can hybridize with miRNA-21 and facilitate their use in quantitative analysis. The extent of hybridization was altered depending on the concentration of the targeted miRNA biomarker that is present in the cancer cells. As the interaction between DNA and miRNA-21 increased, the Forster distance changed, and the spectral overlap underwent a shift. The time-resolved fluorescence decay spectra showed a decrease in the fluorescence lifetime of probe GDQD in the presence of GQDs from 1.99 ns to 0.61 ns, confirming the FRET process [Fig. 3D]. It increased on interaction with DNA due to alterations in the spectral overlap. With increasing distance, the low-intensity GQD emission peak was shifted towards a higher wavelength (λ =505 nm). Thus, the probe showed significant selectivity, good renewability, and high sensitivity for the detection of miRNA-21 in MCF-7 cells [Fig. 3E], The low cytotoxicity of GDQDs provided multicolor imaging of MDA-MB231 cancer cells. Its

Kumar et al. investigated the bioimaging of hypoxic situations closely related to eventual cancer growth using a phosphorescent dyeloaded polymeric nanoparticles-based FRET probe. This approach may overcome challenges such as phototoxicity associated with the generation of reactive oxygen free radical species, poorly resolved in vivo imaging, difficult tracking in dilute systems, and aggregation-caused quenching (ACQ) of physiosorbed dyes. They studied the functioning of a FRET probe developed with 40 nm sized poly (methyl methacrylate-co-methacrylic acid) (PMMA-MA) nanoparticles, which were loaded with (a) blue cyanine dye including an electric double layer of counterion as a donor, and (b) platinum octaethyl porphyrin (PtOEP), an oxygen-sensitive phosphorescent moiety as acceptor nuclei. Approximately 2000 donors for every 20 acceptors in the system provided an efficient FRET process, which could lead to \sim 60-fold enhancement in phosphorescence. This nanoprobe emitted stable fluorescence in addition to red-shifted and oxygen-sensitive phosphorescence; this phenomenon was equivalent in brightness to \approx 1200 PtOEP molecules and provided a ratiometric response to the dissolved oxygen; the high brightness value allowed for oxygen sensing at the single-particle level. The FRET-based oxygen nanoprobe did not show any photobleaching or cytotoxicity incidents upon internalization into affected cells as compared to the incorporation of the PtOEP dye without polymer nanoparticles. This probe enabled multicolor imaging in a HeLa cell culture by in vivo mapping of the dissolved oxygen gradients.

In addition, the combination of FRET and FLIM can provide quantitative information about the donor and acceptor lifetimes in – vivo. 72-81 The association can enable precise distance measurements to evaluate FRET efficiency in cancer cells, mapping of biomolecular interactions, oxygen level monitoring in affected cells, ionic concentration monitoring in affected cells, in vivo monitoring of tumor xenografts, and in vivo monitoring of animal models. Yaghini et al. studied the interaction between an amphiphilic disulfonated aluminum phthalocyanine photosensitizer and Tat-conjugated PEGylated CdSe/ZnS quantum dots (QD) in human breast cancer cells. FRET was observed with the QDs serving as donors; the phthalocyanine photosensitizer mediated the production of singlet oxygen as acceptors. Strong FRET-induced quenching of QDs and photooxidative damage of lysosomal membranes in the cells was recorded by FLIM process.⁷⁹ In another study, Peter et al. employed enhanced green fluorescent protein (EGFP) and the monomeric form of the red fluorescent protein, (mRFP1), as the donor- acceptor pair for FRET - FLIM studies in carcinoma cells in both live- and fixed-cell experiments. They demonstrated interactions between the chemokine receptor (CXCR4) and protein kinase C (PKC) α labeled with EGFP and mRFP1 donor-acceptor moieties. Multiphoton FLI imaging showed the presence of the CXCR4-EGFP: PKCα-mRFP1 complex in proximity to intracellular vesicles and cell protrusions. The FRET process revealed the inability of PKC α to associate with the cytoplasmic portion of CXCR4 in closed form.⁸⁰ Savitsky et al. demonstrated the FLIM – FRET phenomenon for investigating the activity of proteolytic enzyme caspase-3 inside cells. They employed lentivector pLVT with the DNA fragment of TagRFP-23-KFP to enable the transduction of A549 cell lines. The FRET efficiency along with lifetime measurements were studied to understand the possibility of steric restrictions on the reaction between TagRFP-23-KFP and the caspase-3 dimer. An analysis of life-time distributions

from the cell population enabled apoptotic cells and surviving cells to be distinguished within a single frame, which allowed for statistical analysis of drug efficiency.⁸¹

D. Upconverted Luminescence (UCL)

The Anti-Stokes emission pathway has recently grabbed attention for in vivo imaging applications over traditional down conversion emission from organic luminophores and semiconducting quantum dots. 82-95 UCL is a nonlinear optical process in which a molecule absorbs low frequency photons (~900 – 1000 nm) and emits a higher frequency of light (~450 – 600 nm) by subsequent absorption and energy transfer to obtain anti-Stokes luminescence. 96-100,120-122 UCL addresses many challenges in optical imaging, such as tissue autofluorescence, photostability, and cytotoxicity of small molecules by excitation in the NIR region. It can be promoted by continuous wave lasers or common lamps (e.g., low-powered sources); in contrast, femtosecond lasers are required for conventional luminescence. 82-95 Upconverting nanomaterials (UCNPs) remain photostable even after prolonged fluorescence and exhibit negligible toxic to the physiological environment; as such, they are appropriate materials for use in vivo cancer imaging. Luminescent nanoscale lanthanide oxides doped with erbium, thulium, or ytterbium generate upconverting nanoparticles, which have excitation/emission in near-infrared region (NIR). Upconversion can be obtained using probes that exhibit long-lived metastable states to amplify absorption from the second excitation source. 82-95 The lanthanide ions called activators possess several metastable 4f excited states, which are doped in an inorganic crystalline matrix; these materials can serve as an effective UCL emission probe for bioimaging. 84-85 The partly filled 4f shell allows electron delocalization to impart different configurations with variable and high exchange energies, encouraging rich energy levels. Lanthanides exhibit a rich energy level arrangement over a broad range of the electromagnetic spectrum (from NIR to UV). The energy transitions in the 4f level are not affected by the ones occurring in the surrounding host matrices due to effective shielding from 5s and 5p shells outside, which contribute to less vibrational energy losses. 84-85

Upconversion could be achieved through two efficient strategies, which include: (a) two-photon excitation (ground to the metastable state and then to excited state absorption (GSA/ESA)) and (b) energy transfer upconversion (ETU). $^{84-89}$ The former process is based on a single type of lanthanide ion, while the latter one should involve two ions. Therefore, the ESA process for UCL with singly doped lanthanide ions (Tm³⁺, Er³⁺, and Ho³⁺) UCNPs resembles a ladder-like energy level structure. Erbium (Er³⁺), with an energy band gap of about 1.27 eV, shows NIR excitation at ~980 nm and induces three distinct transitions with identical energy photons. $^{91-100,120-124}$ Green emission at approximately 525/545 nm corresponds to the transitions $^2H_{11/2}$ / $^4S_{3/2}$ – $^4I_{15/2}$, and red emission at ~660 nm through the $^4F_{9/2}$ – $^4I_{15/2}$ transition after two-photon absorption. 74 Similarly, Ho³⁺ ions show two main upconversion bands emission at 541 and 647 nm on NIR excitation at nearly 900 nm, which is attributed to the transitions from 5S_2 / 5F_4 – 5I_8 and 5F_5 – 5I_8 , respectively. Tm³⁺ ions show upconversion at a NIR excitation of ~800 nm from 3H_4 \rightarrow 3H_6 transition. 84 This band lies in the "optical transparency window," which

is recommended for imaging of cellular environment, where self-absorption and autofluorescence are controlled. This approach is used for deep tissue imaging in rodents. $^{95-97}$ The specific bands for Tm³⁺ at around 479, 450, and 350 nm are attributed to transitions from 1 G₄ - 3 H₆, 1 D₂ - 3 F₄, and 1 D₂ - 3 H₆. 84 The first UCL strategy involves challenges such as the distance between two similar ions, cross absorption, and concentration, which must be optimized to prevent overall quenching. Thus, the ETU method was desirable to achieve high temporal resolution with strong UCL by doping a sensitizer ion in the host matrix and an activator ion. Several studies suggested the incorporation of Yb³⁺ ions as an efficient sensitizer for enhanced UCL. The absorption maxima lie around 980 nm; the F – F transition of Yb³⁺ resonates with f–f transitions associated with the common upconverting lanthanide ions (Tm³⁺, Er³⁺, and Ho³⁺), which favored the energy flow from Yb³⁺ to these ions [Fig. 4]. 125 Different combinations of these ions could yield multicolor emission upconversion, which may be used for imaging of cancer tissues. $^{95-100, 120-128}$

Li et al. investigated the bioimaging of colorectal carcinoma using peptide-modified UCNPs as biomarkers for cells associated with neovascularization. ¹²⁶ Cancer tumor vessels exhibit certain angiogenic factors, cell adhesion factors, and integrins, which can be targeted for detection using peptide ligands. ⁹⁵⁻⁹⁹ Due to the low possibility of stimulating an immune response and straightforward functionalization, peptides can be considered as dynamic tumor-targeting biomolecules. The visualization of specific interactions of biomarkers directed at tumor cells with high spatial resolution may aid in cancer diagnosis. A luminescence probe containing a carboxyl-terminated silica-coated NaErF 4:Yb@NaGdF4:Yb core@shell was prepared; UCL emission of red light was demonstrated. This material was later modified with two types of peptides containing the PSP motif, 1-SP5-H, and 1-SP5-C; the materials were referred to as UCNP@SiO₂-1-SP5-H and UCNP@SiO₂-1-SP5-C, respectively [Fig. 5A]. The probe was internalized into mouse-bearing tumor cells and was detected with dual mechanism UCL / MR imaging. The UCNP@SiO₂-1-SP5-C probe was noted to provide greater interaction with the HCT 116 tumors; as such, this material may be useful as an image contrast agent for diagnosing HCT 116 tumors [Fig. 5B]. ¹²⁶

Kwon et al. described the fabrication of nanocapsules that were capable of triplet–triplet annihilation upconversion (TTA-UC) for efficient multicolor in vivo imaging in cancer cells. ¹²⁷ The TTA – UC system contained sensitizer and reactive chromophoric centers, in which the former component transferred energy to the latter acceptor chromophore through two stages. The excited acceptor molecules underwent TTA to generate higher energy, low wavelength, and singlet fluorescence even at a low power density of molecule excitation (<10⁻² W cm⁻²). ¹¹⁷ The incorporation of TT –UC chromophores in nanocapsule systems may be able to overcome challenges such as the intervention of triplet oxygen species, the immiscibility of most chromophores in physiological systems, the restricted mobility of conjugated molecules in less porous host matrices, and the lowered energy transfer with fewer intermolecular collisions. They functionalized the nanocapsules with different biomarker peptides to enable differentiation between cancer cells. The immobilized TTA-UC combination emitted two different wavelength radiations, 505 nm (green color) and 470 nm (blue color), with the application of a

single 635 nm excitation (red color). This platform may be able to distinguish the tumor cells belonging to breast and colon cancers in heterogenous cellular environments.¹²⁷

Li et al. synthesized a UCL probe with a dispersion of β-NaYF₄:Yb³⁺, Er³⁺ UCNPs in mesoporous silica nanoparticles (SiO₂). Homogeneous porosity was obtained by the application of cetyltrimethylammonium bromide (CTAB) to SiO₂.¹²⁸ The assembly was treated with polyethylene glycol (PEG) to enable miscibility in an aqueous environment, facilitate cell-specific endocytosis of recognition factors, minimize redundant biological interactions, and enhance physiological stability. The system was further functionalized with folic acid (FA) as a cancer cell targeting biomarker [Fig. 6A].¹²⁸The functionality of the folate-conjugated (UCNPs@mSiO₂-PEG/FA) as well as the unconjugated (UCNPs@mSiO₂-PEG) UCL probe to bind with Hella cells was quantified with ICP – OES measurements with respect to the concentration of Yb³⁺ ions in the cells.¹²⁸ The accumulation of the FA functionalized probe was approximately two-fold higher than the other type. The FA-grafted cells could be readily imaged with a confocal microscope (CLSM). Additionally, UCNPs@mSiO₂-PEG based probes were evaluated for loading with the anti–cancer drug doxorubicin (DOX). They observed that the DOX incubated system (DOX-UCNPs@mSiO₂-PEG/FA) was uniformly dispersed inside the cell cytoplasm and showed strong luminescence with an upconversion effect [Fig. 6B].¹²⁸

Gulzar et al. prepared a multifunctional, nanocomposite UCL probe for bioimaging and theranostic applications. ¹²⁹ Core–shelled UCNPs were modified with nanographene oxide (NGO) and polyethylene glycol; this material was modified with a photosensitizer (PS), chlorin e6 (Ce6). The direct loading of these agents to UCNPs caused minimal UCL emission due to a low quantum yield and an inadequate resonance energy transfer, which quenched the UCNP fluorescence emission. Owing to the high absorption in the NIR window and the efficient agglomeration rate in physiological systems, NGO provided a platform for the dispersion of PSs for noninvasive photodynamic and photothermal therapies (PDT, PTT) in conjugation with PEG. ¹²⁹ UCNPs and NGO were covalently linked via amide bond formation from amino group grafted UCNPs and carboxyl groups attached to NGO. The combined system served as a theranostic probe for use in UCL imaging-directed PDT and PPT for cancer growth visualization and localized treatment. ¹²⁹ The in vivo study used the cell line U14, which was obtained from murine hepatocarcinoma. The nanocomposite NGO-UCNP-Ce6 (labeled as NUC) was internalized into the cells and irradiated with NIR radiation for 5 – 10 min. ⁹ It was observed from hematoxylin and eosin (H & E) stained digital images that NIR- and NUC-treated tumor cells showed a decrease in voluminal size compared to the other groups. ¹²⁹ As such, the combinatorial treatment using laser irradiation (λ=808 nm) and NUC injection exhibited synergistic behavior. Table 1 summarizes the bioimaging probes developed so far.

Table 1. Summary of fabricated bioimaging probes.

Bioimaging	Probe	Cell line / cancer type	Diagnosis	Ref
Technique				
reemiique				
	luminescent dots TNZ2tPPI-Tat NPs	Hepatic cancer cells		33
		MHCC97-H cells,		
		ŕ		
		HeLa cells	Hypochlorite ion (ClO-)	35
	Carbazole (NEC) - tetraphenylethylene (TPE) and thiobarbituric			
	and TDA NEC TDA and TDE TDA			
	acid (TBA), NEC-TBA and TPE-TBA,			
		Tumor growth	Mechanochromism	36
	TCPy and TCPyP, from tetraphenylethene (TPE) and			
	phenylacrylonitrile			
	Boron-dipyrromethene (BODIPY) and triphenylamine (TPA)	PDT / PTT in lysosomes of cancer		37
AIE/ AIE - NIR	Donor acceptor complex	cells	ROS generation	
	Bonot acceptor complex	cens	ROS generation	
	AIE active acrylonitriles TPAT-AN-XF and 2TPAT-AN		Cell imaging	38
		Tumor cells in mouse		
	Red-emissive BODIPY derivatives			39
		Hella cells	Biological processes	
	D. I.			40
	Doxorubicin-conjugated amphiphilic PMPC-PAEMA-P (TPE-			40
	co-HD)-ss-P (TPE-co-HD)-PAEMA-PMPC copolymer	Cancer cells	Tracking intracellular drug delivery	
				41
	Tetraphenylsilole (TPS) unit modified with peptides (caspase-	Cancer cell apoptosis	Overexpression of integrin	
	specific Asp-Glu-Val-Asp (DEVD) and cyclic Arg-Gly-Asp		$\alpha \beta_3$ receptor from U87MG human	
	(cRGD))		glioblastoma cells	
		Renal cell carcinoma (ccRCC)	Lipid droplets-specific bioimaging	42
	Biheteroaryl-bridged probes	tumor cells		
				45
	Folate-functionalized silica shell, 9,10-distyrylanthracene	Hella Cells		
	(DSA)			
	(DSA)			
				l

				6.4
The state of the s	Cetyltrimethylammonium bromide (CTAB) nanomicelles with donor QD - acceptor methylene blue (MB)		Live cell imaging	64
FRET	QD donor - multiple Alexa Fluor 610 (A610) or Alexa Fluor 633 (A633) acceptors			65
	Ratiometric probe (RCP) with Coumarin (donor) – Rhodamine (acceptor)	Mitochondria	-OCl detection	67
	Gold nanoclusters (GNCs) – graphene quantum dot (GQD)	PDT	Singlet oxygen	70
	Pyrido[1,2-a]benzimidazole	Glioma cells	SO ₂ derivatives	109
	Curcumin (CUR) – Nile red (NR) – Polyester nanoparticles (NPs)	Breast cancer cells	Drug release	110
	Quatsome (QS) – Carbocyanine			111
	Rhodamine – 6-hydroxy-2-naphthaldehyde (Rh – HN)	Bioimaging		112
	Lanthanide-based time-gated (TG) probe	In vivo point of care		114
	Polymeric NPs – Photo switchable thermally activated delayed fluorescence (TADF) and Spiro pyran	Oxygenic living cells		115
	Oligo-phenylenevinylene (OPV) – poly caprolactone triblock copolymer – Blue NPs – Nile red	Hella cells / MCF – 7	Bioimaging	116
	Coumarin-cyanoacetic acid (CM) -benzopyrylium (BP)	Mitochondria	GSH/SO ₂	117
	Graphdiyne quantum dots (GDQDs)	MCF – 7	microRNAs-21 (miRNA-21)	118

QDs 525 - Platinum octaethylporphyrin (PtOEP)	Cancer cells	Нурохіа	119
NaYF ₄ :Yb,Er nanocrystals (NCs)	Bioimaging		98
Core shell Er3+ / Tm3+ - Tb3+	Multiplexing bioimaging		120
NaGdF ₄ :Yb,Er nanocrystals	Tumor	MRI / optical imaging	121
NaYF ₄ /NaLuF ₄ : Yb, Er/Tm) - (TTA-UCNPs	Hella cells and small animals	Bioimaging	122
Lanthanide nanophosphors	Bioimaging		123
NaYF ₄ /Yb, Er – Arginine-glycine-aspartic peptide c(RGDFK)	Tumors (ex – vivo / in – vivo)	$\alpha_{V}^{}\beta_{3}^{}$ integrin	124
NaYF ₄ :Yb/Tm@NaYF ₄ :Yb/Er@NaYF ₄ :Yb @NaNdF ₄ :Yb	Bioimaging		125
UCNP@SiO2-L-SP5-H and UCNP@SiO2-L-SP5-C	HCT116 tumors	MR – dual mode imaging	126
TTA-UC nanocapsules		In vitro / in vivo imaging	127
UCNPs@mSiO ₂ -PEG/FA/DOX	-	FA targeted imaging and drug delivery	128
	Cancer cells		
NGO-UCNP-Ce6 (NUC)	Cells and whole animal body	Imaging-guided combinatorial	129
	,	PDT/PTT	
	NaYF ₄ :Yb,Er nanocrystals (NCs) Core shell Er3+ / Tm3+ - Tb3+ NaGdF ₄ :Yb,Er nanocrystals NaYF ₄ /NaLuF ₄ : Yb, Er/Tm) - (TTA-UCNPs Lanthanide nanophosphors NaYF ₄ /Yb, Er - Arginine-glycine-aspartic peptide c(RGDFK) NaYF ₄ :Yb/Tm@NaYF ₄ :Yb/Er@NaYF ₄ :Yb @NaNdF ₄ :Yb UCNP@SiO ₂ -L-SP5-H and UCNP@SiO ₂ -L-SP5-C TTA-UC nanocapsules UCNPs@mSiO ₂ -PEG/FA/DOX	NaYF ₄ :Yb,Er nanocrystals (NCs) Bioimaging Core shell Er3+ / Tm3+ - Tb3+ Multiplexing bioimaging NaGdF ₄ :Yb,Er nanocrystals Tumor NaYF ₄ /NaLuF ₄ : Yb, Er/Tm) - (TTA-UCNPs Hella cells and small animals Lanthanide nanophosphors Bioimaging NaYF ₄ /Yb, Er - Arginine-glycine-aspartic peptide c(RGDFK) Tumors (ex - vivo / in - vivo) NaYF ₄ :Yb/Tm@NaYF ₄ :Yb/Er@NaYF ₄ :Yb @NaNdF ₄ :Yb Bioimaging UCNP@SiO ₂ -L-SP5-H and UCNP@SiO ₂ -L-SP5-C HCT116 tumors TTA-UC nanocapsules UCNPs@mSiO ₂ -PEG/FA/DOX Cancer cells	NaYF ₄ :Yb,Er nanocrystals (NCs) Bioimaging

III. Nanoscale biosensing probes for cancer biomarker detection

Nanoscale materials have been considered for various biosensing applications. ¹³⁰ These materials often exhibit a high surface-to-volume ratio, high surface reactivity, thermal and chemical stability, high catalytic efficacy, and strong absorptivity; for example, immobilization of biological moieties with a desired orientation can lead to enhanced performance (e.g., amplified sensitivity and a much lower detection limit). ¹³¹ Although due to their unique chemical, biological, and physical properties, nanomaterials have been used to detect various biomolecules, including biomarkers for the diagnosis of pancreatic cancer, oral cancer, colorectal cancer, lung cancer, small intestine cancer, breast cancer, brain cancer, and prostate cancer. ^{132,133} These biomarkers can be detected by examining biological fluids, including serum, saliva, urine, blood, and tumor cells. These biomarkers have been utilized for cancer screening, monitoring of therapy, and risk

assessment via point-of-care (POC) devices. For instance, prostate-specific antigen (PSA) is a blood- and semen-based biomarker that is used to detect prostate cancer. 134 Likewise, P53 is another biomarker associated with the unrestricted progression of cells, which can be used to detect bone cancer, ovarian cancer, lung cancer, breast cancer, and leukemia. 135 Similarly, the CD44 biomarker is used to diagnose breast cancer in stem cells. 136 In addition, the cancer antigen 15-3 (CA 15-3) has recently appeared as a potential serum biomarker for breast cancer detection.¹³⁷ Pseudopodium-rich atypical kinase one (PEAK1) has been described as a pancreatic dental adenocarcinoma biomarker that controls cancer growth and cell migration. 138 There are several well-known biomarkers, namely CA 15-3, CA 125, AFP, and CEA, which correspond to different types of lung cancer; these biomarkers can be found in the urine and blood. 139 An important focus area in sensor research is the fabrication of devices for the noninvasive detection of cancer. The goal of these efforts is to replace the existing biomarker screening methods, including polymerase chain reaction (PCR), enzyme-linked immunosorbent assay (ELISA), immunohistochemistry (IHC), western blotting, and radioimmunoassay (RIA). The unique chemical, physical, optical, and electrical properties of various nanoscale materials can enable biomolecule recognition with high sensitivity and specificity. For instance, aggregated gold nanoparticles exhibit an apparent red color, which is noticeable to the naked eye; colloidal gold has been used with immunochromatography approaches for detecting various target antibodies and biomarkers. Similarly, the magnetic properties and large surface area of Fe₃O₄ nanoparticles have been utilized to separate target analytes of lower concentration from complex samples. For example, polymeric nanomaterial decorated with fluorescent tags/dyes has been applied as a label in ELISA. The optical and electronic properties of graphene quantum dots, carbon dots, graphitic carbon nitride quantum dots, and metallic nanocrystals have been utilized to prepare several types of optical and electrochemical sensors. 140-142 In this section, we have highlighted the use of various nanoscale materials for the detection of cancer biomarkers.

Nanotechnology has been utilized in several approaches for diagnosing and treating cancer, including gene therapy, drug delivery, biomarker mapping, molecular imaging, and detection approaches.¹⁵ Nanoscale materials such as nanowires, nanobodies, nanotubes, quantum dots, nanocrystals, metallic nanoparticles, and polymeric materials have been used in these efforts.^{120,121, 143-145} The main challenge in timely cancer detection is the very low level of biomarkers in body fluids during the initial stages of cancer. Nanoscale materials are commonly employed for electrode surface alteration, catalysis, signal amplification, and molecular labeling for the purpose of enhancing biosensing sensitivity. Due to their biocompatibility and large area-to-volume ratio, many types of nanoscale materials have been used to modify sensing electrodes in order to increase the electron transfer capability of the electrodes, enhance the attachment of biological elements to the sensing platform, and reduce the sensing time.^{16,17} Nanomaterials such as noble metals (e.g., Au and Ag NPs), ¹⁴⁶ semiconductor materials (e.g., quantum dots (QDs)), ¹⁴⁷ carbon and graphitic nanomaterials (e.g., carbon nanotubes (CNTs), graphene nanosheets, and graphene oxide (GO)^{16,17}), and nanocomposite materials have been used for the development of electrochemical and optical sensing probes for the early detection of cancer biomarkers.

B. Nanomaterial-based electrochemical probes

In recent years, nanomaterial-based biosensing probes have emerged as materials for the rapid and accurate detection of cancer biomarkers. The sensing probes utilize different biorecognition components, including enzymes, antibodies, ribonucleic acid (RNA), deoxyribonucleic acid (DNA), and target biomolecules, which are attached to the surface of nanomaterial-functionalized electrodes. These electrodes convert biological activity exhibited by the interaction between biorecognition molecules and target biomarkers into measurable electrical or optical signals. Depending on the sensing probes used to convert these signals, the biomarker detection approach can be categorized as either electrochemical biosensing or optical biosensing. Electrochemical and optical biosensors include three main components, namely biorecognition elements that recognize the analyte, signal transducers that convert the biological event into a measurable electrical or optical signal, and a signal processing system. Among these three components, the signal transducers (i.e., working electrodes) are being modified with various types of materials to achieve high sensitivity, high stability, good selectivity, good reproducibility, a wide linearity range, a short analysis time, a low detection limit, and an appropriate lifetime for the intended use.

For example, Kasturi et al. used a naturally reduced rGO/Au nanocomposite to develop an electrochemical biosensor for detecting the microRNA-122 biomarker, which is associated with hepatocellular carcinoma. They used an environment-friendly natural soapnut solution, which was used as a reducing agent for the simultaneous reduction of Au precursor and GO solution to synthesize a rGO/Au nanocomposite. This large and electrochemically active surface area of the freshly prepared GO/Au nanocomposite significantly increased the electron conductivity, leading to an enhanced electrochemical sensing performance. The biosensor exhibited good stability, reproducibility, and a linear response for analyte levels ranging from 10 mM to 10 pM; a lower detection limit of 1.73 pM was demonstrated. They pointed out that the rGO/Au nanocomposite can be easily integrated with a lab-on-a-chip platform for the detection of various biomolecules.

Bharti et al. used a gold platinum bimetallic nanoparticle (AuPtBNPs)/3-aminopropyltriethoxy silane (APTS) nanocomposite as a coating on fluorine-doped tin oxide (FTO) to fabricate a biosensing platform for the detection of miRN-21.¹⁴⁹ In this approach, they hydroxylated the FTO electrode to create -OH moieties on the surface of electrode; this approach provided binding sites for the successful deposition of APTS layer via silane moieties. AuPtBNPs were uniformly electrodeposited on the APTS/FTO electrode using a chronoamperometry technique at -0.2 V potential for 350 s. To immobilize the cDNA probe on the surface of the working electrode, glutaraldehyde was introduced on the surface of AuPtBNPs/APTS/FTO electrode. The cDNA probe decorated electrode (AmcDNA/GA/AuPtBNPs/APTS/FTO) showed good linearity for the detection of miRNA-21 from 1 fM to 100 nM, with the detection limit of 0.63 fM. These results indicated that the conductive nature of metallic nanoparticles (Au and Pt) dramatically increased the sensitivity

and selectivity of the sensing probe due to a synergistic effect. Moon et al. examined a PSA antibody incorporated electropolymerized polypyrrole (Ppy) on a three-dimensional Au nanowire (NW) array for the detection of PSA. They employed an innovative strategy by depositing a Ppy film on AuNW arrays to simultaneously immobilize anti-PSA on each Ppy NW without further modification. This approach provided a large surface area and fine-tuned NW structure for efficient loading of anti-PSA, along with an enhancement in the electron transfer capability of the working electrode. The beneficial electrostatic interaction among the negatively charged carboxyl groups on anti-PSA and the positively charged Ppy chains provided robust immobilization without loss of the antigenic epitope. The immunosensor exhibited enhanced sensing performance, with a linear response for PSA levels from 10 fg/mL to 10 ng/mL. This sensing platform may be merged with standard microfluidic devices for the detection of several biomolecules.

Chammari et al. used a three-component nanocomposite-modified two-screen-printed carbon electrode (2SPCE) array to develop an electrochemical biosensor for the detection of two biomarkers, namely miRNA-21 and cancer-associated CA 15-3.¹⁵¹ The two different redox dye/AuNPs composites, namely toluidine blue-gold nanoparticles and 2,3-diaminophenazine-gold nanoparticles, were used to functionalize the poly(3-aminobenzylamine)/molybdenum selenide/graphene oxide nanocomposite modified 2SPCE array; this material exhibited enhanced electron transfer kinetics for signal generation. Due to the high surface area-to-volume ratio and good conductivity of the nanocomposite, a large number of the biorecognition elements and antibodies were able to be loaded on the functionalized electrodes, leading to efficient and accurate detection of the two cancer biomarkers. The results demonstrated that the biosensing platform provided a reduced detection time, high selectivity, high stability, high reproducibility, simplicity in preparation, and an enhanced limit of detection. Tian et al. used AuNPs and a starch-functionalized multi-walled CNTs nanocomposite functionalized glassy carbon electrode (GCE) to prepare an electrochemical immunosensor to detect PSA. 152 The cross-linked starch functionalization made the multi-walled CNTs positively charged due to the presence of a high number of amino groups, which resulted in the adsorption of the negatively charged Au ion precursor on the surface of starch-functionalized multi-walled CNTs; this approach was used to prepare a homogeneously decorated Au precursor on multi-walled CNTs. The material was reduced using NaBH₄ solution to form AuNPs on multi-walled CNTs. Later, 6 μL of AuNPs/starch-multi-walled CNTs-Nafion suspension was deposited on a pretreated GCE surface; it was dried and washed before the analytical experiments. The immunosensor demonstrated a remarkably low detection limit for PSA of 7 pg/mL.

Kavosi et al. demonstrated a triple signal amplification strategy using polyamidoamine dendrimer encapsulated AuNPs (AuNPs-PAMAM), which were loaded with an enzyme-linked aptamer to create an ultrasensitive electrochemical immunoassay probe for the biomarker PSA.¹⁵³ The strategy involved modifying the GCE with chitosan and a graphene oxide film, followed by covalent attachment of thionine and PSA antibody onto the modified electrode using a glutaraldehyde linker. The detection approach involved a

sandwich-type immunoreaction between the PSA-aptamer and anti-PSA that was immobilized on the chitosan/graphene interface. To further enhance the sensitivity, AuNPs-PAMAM interacted with the PSA-aptamer and HRP-linked aptamer; this sandwich approach was used to record the electrocatalytic reduction of H₂O₂. The PSA biosensor showed excellent sensing performance when tested using prostate tissue and human serum samples. Wu et al. used a novel MXene-Au nanocomposite for the fabrication of an ultrasensitive electrochemical biosensing probe, which was used for the detection of miRNA-377.¹⁵⁴ The synergy between the MXene nanosheet and the AuNPs provided a nanocarrier that demonstrated high electron transfer activity and offered various binding sites for DNA immobilization via Au-S bonds. The guanine-rich sequence DNA recognition probe functionalized AuNPs were used as signal amplification labels, which enhanced the electrochemical signal (2.7-fold). This probe demonstrated superior sensing performance, with a lowest detection limit of 1.35 aM and good linearity ranging from 10 aM to 100 pM. Azimzadeh et al. prepared an ultrasensitive electrochemical nanobiosensor for plasma miR-155 detection using thiolate functionalized Au nanorods (AuNRs) on a GO sheet and GCE. For the fabrication of the sensing probe, they coated the GO sheets on polished GCE, followed by the deposition of AuNRs through an electrostatic interaction. Next, the thiolated single-stranded probe was attached to AuNRs and covered with MCH solution to fill the gaps and alter the orientation for better biomarker recognition. The nanobiosensor exhibited excellent reproducibility, excellent storage ability, a favorable response in real sample analysis, excellent selectivity, and excellent sensitivity.

AgNPs have also been used to develop high-efficiency electrochemical biosensors. For example, Ma demonstrated dual-mode electrochemical sensing of breast cancer biomarkers using core-shell Au@Ag nanorods [Fig. 7A].¹⁵⁶ Au NPs decorated MnO₂ nanosheets were deposited on a GCE, followed by primary antibody immobilization. Next, the modified GCE was incubated with BSA and the analyte biomarker, respectively; later, they incubated the prepared electrode with Au@Ag NRs that were decorated with a secondary antibody. They reported that Au@Ag nanorods were able to catalyze H₂O₂ reduction and intensify the current signal via chronoamperometry. The immunosensor showed good linearity for detection of the cancer biomarker human epidermal growth factor receptor-2 over a concentration from 50 fg/mL to 100 ng/mL; a limit of detection of 16.7 fg/mL was demonstrated. Salahandish et al. developed a label-free nanosensor [Fig. 7B] for detecting miRNA-21 using AgNPs and polyaniline (PANI); this sensor exhibited a wide linear range of 10 fM–10 μM with a lower detection limit of 0.2 fM.¹⁵⁷ The label-free nanosensor was fabricated using AgNPs attached to a modified nanostructured PANI and graphene nanocomposite film; in this approach, three layers of nanocomposite were coated on the electrode surface, followed by the attachment of ss-DNA as a detection probe of miRNA-21. This nanocomposite system permitted more target analytes to be attached at the surface of the electrode, which decreased the space for ion diffusion and electron transfer paths between the nanostructures and the detection probe.

Carbon and graphitic nanomaterials with sizes within the range from 1 nm to 100 nm exhibit several exceptional features, such as intrinsic current mobility, good thermal stability, high electronic conductivity, and excellent mechanical strength. Carbon-based nanomaterials can be readily functionalized and modified; as such, carbon and graphitic nanoprobes have been widely used to fabricate highly efficient electrochemical biosensors for cancer biomarker detection. For instance, Roberts et al. used a highly conductive graphene nanosheet deposited FTO electrode to fabricate an electrochemical sensing platform to detect urokinase plasminogen activator (uPA). The graphene nanosheet-modified FTO surface was used to provide an appropriate immobilization platform for uPAR-Ab and amplify the electrochemical signal because of its higher electrical conductivity. Carbodiimide chemistry was used to immobilize uPAR-Ab on the electrode surface through electrostatic or covalent interactions. They reported that the nanoprobe exhibited a wide detection range (1 fM to 1 µM), good storage stability, repeatability, and reproducibility with a low detection limit (4.8 fM) under optimal conditions.

Okuno et al. used single-walled CNTs array-modified microelectrodes to fabricate a label-free electrochemical biosensing platform, which was used to detect the PSA biomarker. 160 Single-walled CNTs array-modified microelectrodes were incubated with 1pyrenebutanoic acid succinimidyl ester in a dry dimethylformamide solution; covalent immobilization of T-PSA-mAb on the microelectrode surface was subsequently performed. The current signals, which were generated by the oxidation of tryptophan and tyrosine residuals, were enhanced due to the interaction between the covalently immobilized T-PSA-mAb on the surface of singlewalled CNTs and T-PSA. The immunosensor showed a high sensitivity value, with a 0.25 ng/mL detection limit. They pointed out that the cut-off T-PSA value that serves to differentiate between cancer and prostate hyperplasia is ~4 ng/mL; as such, the developed labelfree sensing probe can be considered for clinical applications. Tian et al. used starch-functionalized multi-walled CNTs coupled with AuNPs for the electrochemical detection of PSA. 162 The immunosensor demonstrated good sensitivity towards PSA, with a lowest detection limit of 7 pg/mL and a wide linear range between 0.5 to 3.0 ng/mL. They mentioned that this approach is straightforward and can be used at room temperature without corrosive acids and chemicals. Furthermore, the stability of the developed sensor was greatly improved due to the excellent membrane-forming ability and adsorption capacity of the antibody provided by AuNPs and multi-walled CNTs nanocomposite. Kumar et al. used nanostructured zirconia decorated reduced graphene oxide (rGO) to prepare a label-free and noninvasive electrochemical sensing probe for the detection of CYFRA-21-1, an oral cancer biomarker.¹⁶¹ Nanostructured zirconiacoated rGO was functionalized with APTES prior to electrophoretic deposition of an APTES/zirconia-rGO nanocomposite onto prehydrolyzed ITO glass. Next, a solution mixture of anti-CYFRA-21-1, EDC, and NHS in 2:1:1 ratio was uniformly deposited over APTES/zirconia-rGO/ITO electrode, followed by the blocking of nonspecific active sites using BSA. The sensing platform was validated with an ELISA kit; it exhibited a wide linear range, high sensitivity value (0.756 µA mL/ng), a low detection limit (0.122 ng/mL), and good reproducibility.

Pal and Khan developed an electrochemical immunosensor using AuNPs decorated GO sheets to detect PSA. ¹⁶² Cyclic voltammetry experiments involving bare Pt, modified Au, and Au-GO electrodes showed a diffusion-controlled quasi-reversible electron transfer process. Cyclic voltammetry results also displayed an enhanced current characteristic of Au-GO (more than three times that of Au), which indicated that GO sheets along with AuNPs possess improved conductivity. Hence, the AuNPs decorated GO sheet-based immunosensing platform was tested using human serum samples for the selective and sensitive detection of PSA and found to be highly efficient. Deepa et al. used GO nanoparticles (GrONPs) decorated pencil graphite electrodes (PGE) as an electrochemical sensing probe for the detection of a lung cancer biomarker (CD59). ¹⁶³ To enhance the analytical performance of the PGEs, they used hydroxyl, epoxy, carboxyl, and other reactive oxygen functional groups to enrich the nanomaterial (GrONPs). These oxygen-enriched surface functional groups made the nanocomposite highly hydrophilic and facilitated the chemical functionalization of the surface via covalent bonding. The additional groups increased the electronic conductivity during oxidation-reduction processes involving biomolecules. The GrONPs and PGE composite-based sensing electrode exhibited improved conductivity and high sensitivity towards CD59, with a detection limit of 1 fg/mL.

Luo et al. used a single-walled CNTs@graphene quantum dots (GQDs) nanocomposite [Fig. 7C] as nanocarriers for fabricating a dualsignal amplification non-enzymatic electrochemical sensor to detect a cancer biomarker, namely carcinoembryonic antigen (CEA).¹⁵⁸ They used a nanocomposite of AuNPs and rGO to modify the GCE electrode for the first level of signal amplification, and improved the electrocatalytic properties of the GCE. Next, single-walled CNTs were integrated with GQDs and secondary antibodies to prepare the SWCNTs@GQDs/Ab2 nanocomposites to further amplify the responsive current. Taking advantage of a dual-signal amplification approach, the multifunctional nanocomposite-based biosensing probe exhibited high sensitivity and specificity towards CEA, with a low detection limit of 5.3 pg/mL. Rajaji et al. used iron nitride NPs functionalized multilayer rGO nanosheets to develop an electrochemical biosensing probe for detecting the cancer biomarker 4-nitroquinoline N-oxide. 164 They reported that the excellent conductivity of the rGO nanosheets and the large surface area to volume ratio of the iron nitride NPs provided the nanocomposite probe with excellent sensitivity in real-time human blood and urine samples; a lowest detection limit of 9.24 nM was obtained. This approach may be useful for real-time sensing of other cancer biomarkers. Rauf et al. prepared a highly conductive surface containing a carboxylic group-enriched GO sheet on SPCE for use in a disposable electrochemical immunosensor. 165 The role of GO sheet functionalized on SPCE was to provide immobilization support for antibodies; it also facilitated catalytic signal amplification through methylene blue. Methylene blue was reduced to leuco-methylene blue at the electrode surface; hence, this mechanism was employed to detect protein-antibody interactions. The sensing platform exhibited excellent linearity (0.1 U/mL-2 U/mL) and good performance for Mucin1 biomarker detection in a human serum sample. Due to challenges in device miniaturization and integration of microfluidics technology,

the commercialization of these types of biomarker detection platforms has occurred at a slow pace. Additional studies involving electrochemical transducers are needed to improve the overall stability, performance, efficiency, and reproducibility of the sensing material.

C. Nanomaterials-based optical probes

In the last few years, various types of optical probes have been used for biosensing applications. ^{166,167} These probes demonstrate versatility in terms of receptor type and offer distinct detection mechanisms. ^{168,169} Based on the detection mechanism, nanoscale materials-based optical probes can be categorized into different types such as fluorescence, ^{170,171} surface plasmon resonance (SPR), ¹⁶⁶ and surface-enhanced Raman scattering (SERS). ¹⁷³ Fluorescence permits both imaging and the detection of biomarkers, ^{173–178}; SERS and SPR are utilized for spectroscopic analysis to detect biomolecules. ^{179–181} Due to their fascinating optical, catalytic, and biological properties, nanomaterials have been widely used in the development of optical sensing probes for cancer biomarker detection. ^{182,183} This section highlights the most widely used nanomaterial-based optical probes for cancer biomarker detection.

i. Fluorescence-based optical nanoprobes

Fluorescence-based sensing probes have exhibited high sensitivity, rapid response, good reproducibility, straightforward operation, and high throughput. R2 Many nanomaterials-based fluorescent probes for cancer cell imaging and sensing have been developed; for example, these probes are being considered for early-stage cancer detection. R4 Due to the excellent optical properties and biocompatibility of carbon and graphitic nanomaterials, these materials have garnered attention with regard to the development of fluorescence-based optical sensors for cancer biomarker detection. R5 For instance, Kalkal et al. synthesized amine-functionalized and nitrogen-doped GQDs (amine-N-GQDs) to develop a fluorescent turn-on sensing probe to detect a small cell lung cancer biomarker in an ultrasensitive manner [Fig. 8A]. R6 They used the amine-N-GQDs as an energy donor; AuNPs were utilized as an energy acceptor. In the AuNPs, free electrons in the conduction band offered dipole vectors on the AuNPs surface, which facilitated the acceptance of energy from the donor. The large surface area and broad absorption cross-section values (close to their plasmon resonance) of the AuNPs supported effective energy transfer by taking advantage of the multiple-donor-single-acceptor configuration. The analytical results of the anti-NSE/amine-N-GQDs@AuNPs optical nanoprobe demonstrated a low detection limit (0.009 pg/mL), a wide linear range (0.1 pg/mL to 1000 ng/mL), and a fast response time. The sensing probe was used for the detection of the cancer biomarker in real samples; an acceptable recovery value of 94.69% was demonstrated.

Chen et al. prepared a ratiometric optical sensor using DNA-labeled fluorescent carbon dots (DNA-CDs) and 5,7-dinitro-2-sulfoacridone (DSA) coupling via a target-catalyzing signal amplification approach to detect a cancer biomarker called miRNA-21.186 A optical sensing probe was assembled; they observed that CDs and DNA exhibited a superior fluorescence resonance energy transfer (FRET) efficiency. They demonstrated that a single miRNA-21 can catalyze a disassembly process of multiple CDs with DSA, which altered the fluorescence ratio to detect miRNA-21. The DSA can easily attach to dsDNA via intercalating interactions; a smart biomolecule probe called dsDNA-DSA-CDs was prepared, which reduced the fluorescence intensity of DSA (donors) through the FRET process and increased the emission of CDs (acceptors). The target catalysis signal amplification approach was associated with high sensitivity and a low detection limit (3.0 fM). They reported that this type of ratiometric optical sensing probe may be used to detect multiple target analytes. Nana et al. utilized pentaethylenehexamine and histidine-functionalized GQDs (PEHA-GQD-His) to prepare an optical probe [Fig. 8B]; the nanoplatform was paired with a molecular beacon dual cycle amplification strategy to detect miRNA. 187 In this approach, miRNA was specifically attached to the molecular beacon and activated the target cycle, which led to the nanoassembly process involving the PEHA-GQD-His surface. Photoinduced electron transfer by attaching hemin on the PEHA-GQD-His quenched the fluorescence intensity of the optical sensing probe (PEHA-GQD-His). The optical probe exhibited excellent sensing towards microRNA-141 in human serum, with a lower detection limit of 4.3 × 10⁻¹⁹ M. Al-Ogaidi et al. used GQDs as an energy acceptor to prepare a chemiluminescence resonance energy transfer (CRET) immunosensor that may be used for the selective and rapid detection of an ovarian cancer biomarker (CA-125). 188 The optical sensing probe showed a wide linear range from 0.1 U/mL to 600 U/mL, with a lower detection limit of 0.05 U/mL. In addition to carbon and graphitic nanomaterials, noble metal nanomaterials have been utilized to develop fluorescence-based optical sensing probes for cancer detection. For example, Ma and colleagues developed a label-free novel approach for miRNA detection through enhanced fluorescence intensity of DNA-templated silver nanoclusters (AgNCs) and duplexspecific nuclease-assisted signal amplification (DSNSA). 189 The sequence among the DSNSA, AgNCs, and target miRNA was obtained through the distinctive design of DNA sequences. The DSNSA reaction enabled the release process involving the guanine-rich DNA sequence, which in turn activated the fluorescence of AgNCs through a hybridization process that involves the DNA template. They reported that the fabricated optical probe displayed a wide detection range, good selectivity, and low detection limit (~8.3 fmol).

Likewise, Borghei et al. used DNA-templated fluorescent copper nanoclusters (DNA-CuNCs) to construct an optical sensing probe to monitor the miRNA-155 sequence. ¹⁹⁰ The sensor relied on the shift in the fluorescence intensity of DNA-CuNCs, which is caused by specific miRNA binding-155. They mentioned that under optimized conditions, the sensing platform exhibited a broad linear detection range (50 pM to 10 nM) with a lower detection limit of 11 pM; excellent sensing towards miRNA in human plasma and saliva samples was demonstrated. Zhang et al. used silicon nanodots (SiNDs) as an optical sensing platform for detecting the mucin-1 biomarker. ¹⁹¹

An aptasensor with high sensitivity was developed through the covalent interaction of fluorescent SiND and cyanine (Cy5)-tagged aptamer S2.2.

Similarly, Hernot et al. discussed the efficiency of an IR800 dye-conjugated fluorescent anti-CEA nanobody for imaging of pancreatic cancer xenografts in a mouse model. They observed that the intravenously administered nanobodies can rapidly localize the tumors within an hour. In another study, Hernot et al. demonstrated the in vivo optical imaging potential of a novel fluorescent molecule (S775Z) labeled single-domain antibody for targeted visualization of a universal tumor marker in subcutaneous and orthotopic tumor models with medically acceptable target-to-background ratios. 192-193

ii. SPR-based optical nanoprobes

SPR-based optical sensors have garnered considerable interest in healthcare applications because of their ability to provide nondestructive, label-free, and high-sensitivity detection of biomolecules. 194 SPR-based sensing probes have been used for the detection of several types of biomolecules; however, the analysis of cancer biomarkers using SPR has garnered less attention. The use of novel nanomaterials and nanocomposites in SPR-based sensors has enhanced the selectivity and sensitivity of these devices. The unique characteristics of nanomaterials, such as high specific surface area, biocompatibility, ease of functionalization, alterations in the refractive index, and improvements in signal amplification, may improve the sensing functionality of optical sensors. 197 Metal NPs have mainly been used for SPR-based analysis of cancer biomarkers due to their high levels of electrical conductivity and chemical inertness. Several SPR-based sensors containing AuNPs have been used to identify cancer biomarkers and are being used to improve SPR performance. For instance, Wang et al. developed [Fig. 9A] a sensitive aptamer-based sensor for cancer exosome detection through an SPR technique using dual AuNPs-assisted signal amplification. 195 Nanoparticles-based dual amplification was obtained by regulated attachment of AuNPs, which offered electronic coupling among Au film and AuNPs. They mentioned that 11-mercapto-1-undecanol (MCU) was used for suppression of the nonspecific adsorption of AuNPs on the SPR surface; regeneration of the SPR signal was achieved. The developed sensor exhibited a 104-fold enhancement in the detection limit when compared with ELISA.

Zhang et al. demonstrated the SPR effect of Au nanorods (AuNRs) by altering the thickness of SiO₂ in a AuNRs@SiO₂ nanocomposite for the detection of miRNAs [Fig. 9B]. ¹⁹⁶ They decorated a silica shell on AuNRs, followed by adsorption of the UCNPs onto the silica shell through electrostatic interaction. The existence of a silica shell prevented unwanted energy transfer because of direct contact between UCNPs and AuNRs. The results revealed an enhancement factor of approximately fifty times and excellent sensing in human serum samples and cancer cell (MCF-7) lysates. Fiber optic-based SPR sensing platforms exhibit several advantages, such as the capability for remote use and miniaturization for real-time use. For example, Wattiez et al. constructed a fiber optic-based SPR (OF-SPR) sensing probe to detect the biomarker HER2 using 400 μm core- diameter optical fibers coated with a gold film. ¹⁹⁸ They decorated the gold surface with anti-HER2-ssDNA to bio-functionalize the fiber, which enabled the HER2 antibodies to be attached to HER2

proteins; this approach enhanced the signal because of the mass effect. Hence, utilization of such a sandwich approach (aptamer-HER2-HER2 antibody) enhanced the movement of SPR and exhibited high sensitivity towards the HER2 biomarker. This approach may be used for multiplexed sensing, in which distinct fibers functionalized with different receptors are placed in a side-by-side manner.

iii. SERS-based optical nanoprobes

The SERS-based sensing probe relies on the inelastic collisions that take place due to the interaction of electromagnetic fields with molecules. In this approach, the photons that produce the electromagnetic fields either lose or gain the energy from the molecules, leading to the shift in the scattered photon frequency. This change in the frequency of the incident light observed in the scattered photon is called the Raman shift. Although the Raman scattering (10⁻⁶ of the incident light intensity) shows poor intensity for some materials, the inelastic light scattering was found to be significantly increased (up to 10⁸ or even higher) for AgNPs and AuNPs. The surface of these metal nanoparticles becomes excited and creates high-density "hot spots," which significantly enhance the Raman scattered signal. Additionally, its nondestructive nature and capability for accommodating fiber optic technology make the SERS-based optical sensing technique a promising approach for real-time applications. Various materials have been used in the development of efficient SERS platforms to markedly enhance the SERS signal, such as core-shell nanostructures, composite nanostructures, and some hybrid materials. Among all, metal nanostructures have been widely utilized to create SERS platforms because of their well-controlled sizes and shapes.

For example, Wang et al. used AgNPs and multiplex reverse transcription-recombinase polymerase amplification (RT-RPA) for the development of a label-free optical SERS sensing probe [Fig. 10A] to directly detect multiple RNA biomarkers. ²⁰⁸⁻²⁰⁹ They mentioned that after extraction of RNA from urine samples, the target RNA biomarkers were amplified using isothermal RT-RPA and subsequently stabilized in the form of dsDNA amplicons. After purification and amplification, the obtained amplicons were mixed with SERS substrates (AgNPs); Raman spectra were subsequently obtained. The sensing probe exhibited 95.3% sensitivity, 93.0% specificity, and 94.2% accuracy. SERS platforms can sometimes exhibit uneven distribution, formation of aggregates, and accumulation in benign tissues; these phenomena may complicate the interpretation of the results. In another study, Song et al. concurrently stacked two Raman active probes on core-shell designed Au nanomaterials [Fig. 10B]. ⁸⁵ In this approach, one molecule was used to obtain the detection signal; the other one provided the reference value. Further, the ratio of these signals was utilized to identify the concentration of the cancer biomarker. These optical sensing techniques offer a straightforward, rapid, reliable, and economical approach to detect cancer. In recent years, many types of optical sensing probes have been developed using nanoscale materials for the sensitive detection of cancer biomarkers in human serum and blood samples; however, many shortcomings involving optical sensing probes that need to be addressed.

For example, real-time biofluids are complex mixtures; as such, the optical signals produced by nanostructured materials are highly susceptible to interaction with various components in these complex mixtures. More accurate and controlled synthesis of nanomaterials and better surface modification approaches are necessary to increase the stability, sensitivity, and specificity of sensing probes toward the target analytes in complex biofluid samples.

IV. Conclusions and future outlook

In this review, we discussed several tools for the integrated early diagnosis of cancer proliferation. The review considered bioimaging and biosensing as the two main approaches for cancer cell tracking. An emphasis of the review was a consideration of the features of fluorescence microscopy as a streamlined live cell imaging technique, along with a brief investigation of its gradual evolution over time. In addition, the main photophysical mechanisms responsible for FM operations were explained. AIE, PET, FRET, and UCL-based imaging probes were considered, focusing on the clinical implementations of these processes. The efficiency of AIEgens has been demonstrated for tumor imaging via various studies. AIEgens are limited by issues such as high energy photon excitation, background illumination, and the absence of multimodal recognition of the cellular environment. Several strategies, such as combinatorial approaches, have been described to overcome these challenges. Other than the value added AIEgen 102 discussed here, Zhang et al. reported on a formulation with a tris(hydroxypropyl)phosphine (THPP) derivative of boron dipyrromethene (BODIPY), a stable NIR— II AIEgen with excitation maxima at ~980 nm and a high molar extinction coefficient (~2.1 x 10⁵). The J-aggregated form could enhance the brightness with bathochromic shift, which enables the visualization of pro-oncological tissues, invasive dysplasic tissues, and cerebral vasculature. 44 Song et al. developed a NIR-II AIEgen for sentinel lymph node (SLN) imaging with bright fluorescence from excitation at 920 nm. Since it exhibits a high signal-to-background ratio and penetration depth, this approach can serve as an in vivo imaging approach for tumor staging and surgical navigation of SLN.²¹⁰ Fang et al. designed a three-photon NIR-activated AIEgen based on a dithiol platinum (Pt II) complex (Lyso-Pt-CH₃), which included a phenyl pyridine (ppy) moiety. Lyso-Pt-CH₃ can assist the threephoton fluorescence (3PF) process due to intramolecular charge transfer in the twisted configuration, resulting in high spatial tumor imaging. Further, the PET process was noted to generate selective fluorescence with better-resolved images based on a successive 'offon-off mechanism. Improved PET probes were developed by Chu et al. using DDO (dicloro-dicyano-benzoquinone) and a thiol derivative of pyrrole called BSP.60 These materials may be used to detect the uncontrolled release of HOCl in malignant tissues. The efficiency of the emissive FRET process is primarily governed by an efficient spectral overlap and the relative dipole orientation of the donor and acceptor molecules in the vicinity. Other disadvantages, such as tissue autofluorescence and an inhomogeneous distribution of analyte, can complicate the detection of affected cells. Recently developed ratio metric FRET probes could compensate for these limitations. Likewise, Chung et al. developed a ratiometric FRET probe as a copper indicator, which involved a chemo-selective conversion of Cu (I) - Cu (II) along with oxidative cleavage of C-O in the tris[(2-pyridyl) methyl] amine (TPA) molecule. Since the

dysregulation of the cellular Cu^{2+/+} ion is closely related to the oncogenic conversion of glutathione, the FRET probe could selectively image cancer proliferation via the labile copper pools that are present in affected cells. ²¹²⁻²¹³ Further, the UCL probes exhibit unique emission properties, which can address the limitations associated with other photophysical mechanisms. UCL probes allow for multimodal emissions and high upconversion efficiencies, with potential modifications in lanthanide ion composition and fluorophore encapsulation in host matrices. Considerable efforts have been made so far to develop UCL-based multifunctional bioimaging probes; however, considerations such as complete dispersibility in physiological systems may limit the use of these materials. Tan et al. recently considered up-converted bioimaging with pH-triggered and water-dispersible NIR upconversion NPs (NRhD-PEG-X NPs). Acidic pH and NIR excitation at ~810 nm activated photothermal upconversion, which could enable the emissive fluorescence image—guided cancer cell therapy. ²¹⁴⁻²¹⁵ Additional studies must be undertaken to develop wastewater-miscible CL probes for enhanced non-invasive cancer growth imaging.

In addition, the use of various cancer biomarkers as biorecognition elements as well as nanoscale materials as electrode surface modifiers, catalysts, and signal amplifiers for electrochemical and optical biosensing has been reviewed. Due to their biocompatibility and large area-to-volume ratio, different types of nanoscale materials such as semiconductor materials (e.g., quantum dots, QDs), noble metal (e.g., Ag NPs and Au NPs), carbon and graphitic nanomaterials (e.g., graphene oxide (GO), carbon nanotubes (CNTs), and graphene nanosheets), as well as other nanocomposite materials have been extensively studied to modify the surface of the working electrode. Modification and functionalization procedures can enhance the electron transfer capability of the electrodes and the analytical performance of the sensors. Although the potential of nanoscale materials for cancer diagnosis has been demonstrated over several years, several challenges must be addressed to facilitate clinical translation of these materials, such as (a) synthesis of nanoscale materials with reproducible chemical, biological, electrical, and optical properties, (b) improved surface modification processes to minimize the nonspecific absorption of biomolecules and enhance the stability of biosensor in complex samples, and (c) development of novel cancer biomarkers for serum, saliva, urine, blood, and tumor cells that can support the early diagnosis of various types of cancers.

Acknowledgments

R.J.N. wishes to acknowledge support from National Science Foundation Grant # 2029974.

References

- ¹I. Gómez, J. Seoane, P. Varela-Centelles, P. Diz, and B. Takkouche, Eur. J. Oral Sci. 117, 541 (2009).
- ²S. Chen, H. Wu, N. Lv, H. Wang, Y. Wang, Q. Tang, H. Shao, and C. Sun, Biomed. Pharmacother. 82, 583 (2016).
- ³C.H. Chang, and S. Pauklin, J. Exp. Clin. Cancer. Res. 40, 1 (2021).
- ⁴K. Zeng, X. Xu, M.U. Chen, X. Liu, X. Hu, T. Xu, H. Sun, Y. Pan, B. He, and S. Wang, Cell Death Dis. 9, 1 (2018).
- ⁵J. Folkman, In Seminars in oncology (Elsevier, WB Saunders, 2002) 29
- ⁶D. Ghosh, and M.R. Dawson, *Biomechanics Oncol*. (Springer, Cham, 2018) 1092.
- ⁷P. Hadji, R. Coleman, M. Gnant, and J. Green, Ann. Oncol. 23, 2782 (2012).
- ⁸W. Wang, H.J. Chu, Y.C. Liang, J.M. Huang, C.L. Shang, H. Tan, D. Liu, Y.H. Zhao, T.Y. Liu, and S.Z. Yao, Tumor Biol. **37**, 14873 (2016).
- ⁹C.L. Hsieh, Z. Xie, J. Yu, W.D. Martin, M.W. Datta, G.J. Wu, and L.W. Chung, The Prostate. 67, 685 (2007)
- ¹⁰P.C. Pandey, M.D. Mitra, S. Shukla, and R.J. Narayan, Biosensors. 11, 122 (2021).
- ¹¹P.C. Pandey, H.P. Yadav, S. Shukla, and R.J. Narayan, Chemosensors, 9, 253 (2021).
- ¹²M.A. Mycek and B.W. Pogue, *Handbook of biomedical fluorescence*, 1st ed. (T & F, Boca Raton, 2003), 694.
- ¹³K. Berg, P.K. Selbo, A. Weyergang, A. Dietze, L. Prasmickaite, A. Bonsted, B.Ø. Engesaeter, E. Angell-Petersen, T. Warloe, N. Frandsen, and A. Høgset, J. Microsc. **218**, 133 (2005).
- ¹⁴T. Ishizawa, N. Fukushima, J. Shibahara, K. Masuda, S. Tamura, T. Aoki, K. Hasegawa, Y. Beck, M. Fukayama, and N. Kokudo, Cancer. **115**, 2491 (2009).
- ¹⁵ C. Jin, K. Wang, A. Oppong-Gyebi, and J. Hu, Int J Med Sci 17, 2964 (2020).
- ¹⁶ G. Valenti, S. Scarabino, B. Goudeau, A. Lesch, M. Jović, E. Villani, M. Sentic, S. Rapino, S. Arbault, F. Paolucci, and N. Sojic, J Am Chem Soc 139, 16830 (2017).
- ¹⁷ S. Zhang and Y. Liu, Front Chem **8**, 626243 (2021).
- ¹⁸K. Tawa, S. Yamamura, C. Sasakawa, I. Shibata, and M. Kataoka, ACS Appl. Mater. Interfaces. 8, 29893 (2016).
- ¹⁹G. Wang, M. Zannikou, L. Lofchy, Y. Li, H. Gaikwad, I.V. Balyasnikova, and D. Simberg, ACS Nano. 15, 11880 (2021).
- ²⁰H. Blom, and J. Widengren, Stimulated emission depletion microscopy. Chem. Rev. **117**, 7377 (2017).
- ²¹H. Yang, Y. Wu, H. Ruan, F. Guo, Y. Liang, G. Qin, X. Liu, Z. Zhang, J. Yuan, and X. Fang, Anal. Chem. **94**, 3056 (2022).
- ²²P. Charalampaki, M. Nakamura, D. Athanasopoulos, and A. Heimann, Front. Oncol. 9, 583 (2019).
- ²³J. Dobbs, S. Krishnamurthy, M. Kyrish, A.P. Benveniste, W. Yang, and R. Richards-Kortum, Breast Cancer Res. Treat. **149**, 303 (2015).
- ²⁴J.A. Barreto, W. O'Malley, M. Kubeil, B. Graham, H. Stephan, and L. Spiccia, Adv. Mater. 23, H18 (2011).

- ²⁵G. Hong, A.L. Antaris, and H. Dai, Nat. Biomed. Eng. 1, 1 (2017).
- ²⁶H.S. Choi, S.L. Gibbs, J.H. Lee, S.H. Kim, Y. Ashitate, F. Liu, H. Hyun, G. Park, Y. Xie, S. Bae, and M. Henary, Nat. Biotechnol. **31**, 148 (2013).
- ²⁷Y. Liu, Q. Chen, Y. Sun, L. Chen, Y. Yuan, and M. Gu, E. R. **2**, 206, (2021)
- ²⁸J. Qi, C. Sun, A. Zebibula, H. Zhang, R.T. Kwok, X. Zhao, W. Xi, J.W. Lam, J. Qian, and B.Z. Tang, Adv. Mater. **30**, 1706856 (2018).
- ²⁹J. Zhang, H. Zou, S. Gan, B. He, J.C. Huang, C. Peng, J.W. Lam, L. Zheng, and B.Z. Tang, Adv. Funct. Mater. **32**, 2108199 (2022).
- ³⁰Y. Hong, J.W. Lam, and B.Z. Tang, Chem. Comm. **29**, 4332 (2009)
- ³¹J. Mei, Y. Hong, J.W. Lam, A. Qin, Y. Tang, and B.Z. Tang, Adv. Mater. **26**, 5429 (2014).
- ³²H. Lu, Y. Zheng, X. Zhao, L. Wang, S. Ma, X. Han, B. Xu, W. Tian, and H., Gao, Angew. Chem. Int. Ed. **55**, 155 (2016).
- ³³M. Teng, Y. Chen, Y. Xie, Z. Li, O. Wan, Z. Wang, and J. Yang, Dyes Pigm. **195**, 109679 (2021).
- ³⁴Y.F. Wang, T. Zhang, and X.J. Liang, Small. **12**, 6451 (2016).
- ³⁵H. Chen, X. He, Y. Yu, Y. Qian, J. Shen, and S. Zhao, Talanta, **214**, 120842 (2020).
- ³⁶X. Yang, Q. Wang, P. Hu, C. Xu, W. Guo, Z. Wang, Z. Mao, Z. Yang, C. Liu, G. Shi, and L. Chen, Mater. Chem. Front. 4, 941 (2020).
- ³⁷M. Yang, J. Deng, H. Su, S. Gu, J. Zhang, A. Zhong, and F. Wu, Materials Chemistry Frontiers, 5, 406 (2021).
- ³⁸G. Niu, X. Zheng, Z. Zhao, H. Zhang, J. Wang, X. He, Y. Chen, X. Shi, C. Ma, R.T. Kwok, and J.W. Lam, JACS. **141**, 15111 (2019).
- ³⁹W. Che, L. Zhang, Y. Li, D. Zhu, Z. Xie, G. Li, P. Zhang, Z. Su, C. Dou, and B.Z. Tang, Anal. Chem **91**, 3467 (2019).
- ⁴⁰X. Su, B. Ma, J. Hu, T. Yu, W. Zhuang, L. Yang, G. Li, and Y. Wang, Bioconjug. Chem. **29**, 4050 (2018).
- ⁴¹D. Ding, J. Liang, H. Shi, R.T.K. Kwok, M. Gao, G. Feng, Y. Yuan, B.Z. Tang, and B. Liu, *J. Mat. Chem. B.* 2, 231 (2014).
- ⁴²P. Tan, C. Li, Y. Wang, W. Zhuang, M. Chen, L. Zhou, J. Zhang, Q. Gong, Q. Wei, and J. You, Dyes Pigm. **188**, 109215 (2021).
- ⁴³R. Long, C. Tang, Q. Wei, C. Tong, X. Tong, S. Shi, Y. Guo, and Y. Yang, Sens. Actuators. Chem. **348**, 130666 (2021).
- ⁴⁴O. Zhang, P. Yu, Y. Fan, C. Sun, H. He, X. Liu, L. Lu, M. Zhao, H. Zhang, and F. Zhang, Angew. Chem. **133**, 4013 (2021).
- ⁴⁵Z. Wang, B. Xu, L. Zhang, J. Zhang, T. Ma, J. Zhang, X. Fu, and W. Tian, Nanoscale. 5, 2065 (2013).
- ⁴⁶A.P., De Silva, H.N. Gunaratne, T. Gunnlaugsson, A.J. Huxley, C.P. McCoy, J.T. Rademacher, and T.E. Rice, Chem. Rev. **97**, 1515 (1997).
- ⁴⁷A.P., De Silva, T.S. Moody, and G.D. Wright, Analyst. **134**, 2385 (2009).
- ⁴⁸S. Doose, H. Neuweiler, and M. Sauer, ChemPhysChem, **10**, 1389 (2009).
- ⁴⁹T., Nagano, Proc. Jpn. Acad., Ser. B, Phys. **86**, 837-847 (2010).
- ⁵⁰W., Zhang, Z., Ma, L. Du, and M. Li, Analyst. **139**, 2641 (2014).
- ⁵¹ B. Daly, J. Ling, and A.P. De Silva, Chem. Soc. Rev. **44**, 4203 (2015).
- ⁵²Y. Tang, D. Lee, J. Wang, G. Li, J. Yu, W. Lin, and J. Yoon, Chem. Soc. Rev. **44**, 5003 (2015).

- ⁵³K.J. Mintz, B. Guerrero, and R.M. Leblanc, J. Phys. Chem. C. **122**, 29507 (2018).
- ⁵⁴H.H. Deng, K.Y. Huang, S.B. He, L.P. Xue, H.P. Peng, D.J. Zha, W.M. Sun, X.H. Xia, and W. Chen, Anal. Chem. **92**, 2019 (2019).
- ⁵⁵M. Mahani, P. Karimi-Mazidi, F. Khakbaz, and M. Torkzadeh-Mahani, Microchim. Acta. 189, 1 (2022).
- ⁵⁶H. Zhang, J. Fan, K. Wang, J. Li, C. Wang, Y. Nie, T. Jiang, H. Mu, X. Peng, and K. Jiang, Anal. Chem. **86**, 9131 (2014).
- ⁵⁷H. Zhu, H. Zhang, C. Liang, C. Liu, P. Jia, Z. Li, Y. Yu, X. Zhang, B. Zhu, and W. Sheng, Analyst. **144**, 7010 (2019).
- ⁵⁸S. Shukla, S. Singh, and M.D. Mitra, ChemistrySelect. **5**, 13609 (2020).
- ⁵⁹L. Zhou, J. Cui, Z. Yu, D. Zou, W. Zhang, and J. Qian, Sens. Actuators Chem. **332**, 129494. (2021).
- ⁶⁰C.J. Chu, G.S. Wu, H.I. Ma, P. Venkatesan, N. Thirumalaivasan, and S.P. Wu, SAA. **233**, 118234 (2020).
- ⁶¹H. Sahoo, J. Photochem. Photobiol. **12**, 20 (2011).
- ⁶²G. Chen, F. Song, J. Wang, Z. Yang, S. Sun, J. Fan, X. Qiang, X. Wang, B. Dou, and X. Peng, Chem Comm. 48, 949 (2012).
- ⁶³Y.J. Gong, X.B. Zhang, C.C. Zhang, A.L. Luo, T. Fu, W. Tan, G.L. Shen, and R.Q. Yu, Anal. Chem. **84**, 10777 (2012).
- ⁶⁴L. Li, J. Liu, X. Yang, Z. Peng, W. Liu, J. Xu, J. Tang, X. He, and K. Wang, Chem. Comm. **51**, 14357 (2015).
- ⁶⁵E.M. Conroy, J.J. Li, H. Kim, and W.R. Algar, J. Phys. Chem. C. **120**, 17817 (2016).
- ⁶⁶B. Wallace, and P.J. Atzberger, PLoS One. 12, e0177122 (2017).
- ⁶⁷S.L. Shen, X. Zhao, X.F. Zhang, X.L. Liu, H. Wang, Y.Y. Dai, J.Y. Miao, and B.X. Zhao, J. Mater. Chem. B. 5, 289 (2017).
- ⁶⁸Pandey, P.C. and S. Shukla, ASEM. **8**, 271 (2016).
- ⁶⁹P. Raidev, and S. Ghosh, J. Phys. Chem. **123**, 327 (2018).
- ⁷⁰A. Vangara, A. Pramanik, Y. Gao, K. Gates, S. Begum, and P. Chandra Ray, ACS Appl. Bio. Mater. 1, 298 (2018).
- ⁷¹ D. Zhang, A. Liu, R. Ji, J. Dong, and Y. Ge, Anal. Chim. Acta. **1055**, 133 (2019).
- ⁷²K. Abe, L. Zhao, A. Periasamy, X. Intes, and M. Barroso, PloS one. **8**, e80269 (2013).
- ⁷³H. Wallrabe, Z. Svindrych, S.R. Alam, H.H. Siller, T. Wang, D. Kashatus, S. Hu, and A. Periasamy, Sci. Rep. 8, 79 (2018).
- ⁷⁴M. Barroso, M.G. Monaghan, R. Niesner, and R.I. Dmitriev, Adv. Drug. Deliv. Rev. 115081 (2023).
- ⁷⁵ N. O'Donnell, and R. I. Dmitriev, Multi-parametric Live Cell Microscopy of 3D Tissue Models. (Springer International Publishing, Berlin, Germany, 2017), p. 49.
- ⁷⁶I. A. Okkelman, J. Puschhof, D. B. Papkovsky, and R. I. Dmitriev, Intestinal Stem Cells: Methods and Protocols (Humana, New York, NY, 2020), p. 65.
- ⁷⁷H. Wallrabe, and A. Periasamy, Curr. Opin. Biotechnol. **16**, 19 (2005).
- ⁷⁸H. Wallrabe, Z. Svindrych, S.R. Alam, K.H. Siller, T. Wang, D. Kashatus, S. Hu, and A. Periasamy, Sci. Rep. 8, 79 (2018).
- ⁷⁹E. Yaghini, F. Giuntini, I.M. Eggleston, K. Suhling, A.M. Seifalian, and A.J. MacRobert, Small. **10**, 782 (2014).
- ⁸⁰A.P. Savitsky, A.L. Rusanov, V.V. Zherdeva, T.V. Gorodnicheva, M.G. Khrenova, and A.V. Nemukhin, Theranostics. **2**, 215 (2012).

- 81M. Peter, S.M. Ameer-Beg, M.K. Hughes, M.D. Keppler, S. Prag, M. Marsh, B. Vojnovic, and T. Ng, Biophys. J. 88, 1224 (2005).
- ⁸²J.M. Meruga, A. Baride, W. Cross, J.J. Kellar, and P.S. May, J. Mater. Chem. C. 2, 2221 (2014).
- ⁸³Y., Wang, K. Zheng, S. Song, D. Fan, H. Zhang, and X. Liu, Chem. Soc. Rev. 47, 6473 (2018).
- ⁸⁴X. Li, F. Zhang, and D. Zhao, Chem. Soc. Rev. 44, 1346 (2015).
- 85P. Joshi, P.R. Riley, W. Denning, S. Shukla, N. Khosla, J. Narayan, and R. Narayan, J. Mater. Chem. C. 10, 2965 (2022).
- ⁸⁶S. Han, R. Deng, Xie, X. and X. Liu, Angew. Chem. Int. Ed. **53**, 11702 (2014).
- ⁸⁷Pandey, P.C., Shukla, S., Pandey, G. and Narayan, R.J., 2020. MRS Adv. 5, pp.2429-2444.
- ⁸⁸J. Zhou, Q. Liu, W. Feng, Y. Sun, and F. Li, Chem, Rev. **115**, 395 (2015)
- ⁸⁹A. Nadort, J. Zhao, and E.M. Goldys, Nanoscale. **8**, 13099 (2016).
- ⁹⁰N. Joshi, S. Shukla, and R.J. Narayan, TBIO. e202200001 (2022).
- ⁹¹G. Wang, Q. Peng, and Y. Li, JACS. **131**, 14200 (2009).
- 92P. Joshi, S. Shukla, S. Gupta, P.R. Riley, J. Narayan, and R.J. Narayan, ACS Appl. Mater. Interfaces. 14, 37149 (2022).
- ⁹³J. Yao, C. Huang, C. Liu, and M. Yang, Talanta. **208**, 120157 (2020).
- 94S. Shukla, R.H. Huston, B.D. Cox, A.R. Satoskar, and R.J. Narayan, Expert Opin Drug Deliv. 19, 1505 (2022).
- ⁹⁵J. Bergstrand, Q. Liu, B. Huang, X. Peng, C. Würth, U. Resch-Genger, Q. Zhan, J. Widengren, H. Ågren, and H. Liu, Nanoscale. **11**, 4959 (2019).
- ⁹⁶S. Shukla, P. Joshi, P. Riley, and R.J. Narayan, Biosens, Bioelectron. **216**, 114592 (2022).
- ⁹⁷D. Matsuura, Appl. Phys. Lett. **81**, 4526 (2002).
- 98 J. Zhao, Z. Lu, Y. Yin, C. McRae, J.A. Piper, J.M. Dawes, D. Jin, and E.M. Goldys, Nanoscale. 5, 944 (2013).
- ⁹⁹H. Li, X. Wang, T.Y. Ohulchanskyy, and G. Chen, Adv. Mater. **33**, 2000678 (2021).
- ¹⁰⁰X. Xie, N. Gao, R. Deng, O. Sun, O.H. Xu, and X. Liu, JACS, **135**, 12608 (2013).
- ¹⁰¹F. Hu, Y. Huang, G. Zhang, R. Zhao, H. Yang, and D. Zhang, Anal. Chem. **86**, 7987 (2014).
- ¹⁰²F. Tang, J.Y. Liu, C.Y. Wu, Y.X. Liang, Z.L. Lu, A.X. Ding, and M.D. Xu, ACS Appl. Mater. Interfaces. 13, 23384 (2021).
- ¹⁰³M. Pirsaheb, S. Mohammadi, and A. Salimi, *TrAC Trends*. Anal. Chem. **115**, 83 (2019).
- ¹⁰⁴F. Liao, X. Song, S. Yang, C. Hu, L. He, S. Yan, and G. Ding, J. Mater. Chem. A. **3**, 7568 (2015).
- ¹⁰⁵W.C. Silvers, B. Prasai, D.H. Burk, M.L. Brown, and R.L. McCarley, *JACS.* **135**, 309 (2013).
- ¹⁰⁶X. Huang, M. Lan, J. Wang, L. Guo, Z. Lin, F. Zhang, T. Zhang, C. Wu, and B. Qiu, Anal. Chim. Acta. **1142**, 65 (2021).
- ¹⁰⁷W., Sun, M. Li, J. Fan, and X. Peng, Acc. Chem. Res. **52**, 2818 (2019).
- ¹⁰⁸C. Du, S. Fu, X. Wang, A.C. Sedgwick, W. Zhen, M. Li, X. Li, J. Zhou, Z. Wang, H. Wang, and J.L. Sessler, Chem. Sci. **10**, 5699 (2019).

- ¹⁰⁹C. Chen, Y. Yao, W. Wang, L. Duan, W. Zhang, and J. Qian, SAA. **241**, 118685 (2020).
- ¹¹⁰S. Saxena, A. Pradeep, and M. Jayakannan, ACS App Bio. Mater. 2, 5245 (2019).
- 111 J. Morla-Folch, G. Vargas-Nadal, T. Zhao, C. Sissa, A. Ardizzone, S. Kurhuzenkau, M. Köber, M. Uddin, A. Painelli, J. Veciana, and
- K.D. Belfield, ACS Appl. Mater. Interfaces 12, 20253 (2020).
- ¹¹²X. He, F. Ding, W. Xu, C. Xu, Y. Li, Y. Qian, S. Zhao, H. Chen, and J. Shen, Anal. Chim. Acta. **1127**, 29 (2020).
- ¹¹³S. Miao, K. Liang, and B. Kong, Mater. Chem. Front **4**, 128 (2020).
- ¹¹⁴X. Qiu, J. Xu, M. Cardoso Dos Santos, and N. Hildebrandt, Acc. Chem. Res. 55, 551 (2022).
- ¹¹⁵M. Yu, W. Zhao, F. Ni, Q. Zhao, and C. Yang, Adv. Opt. Mater. **10**, 2102437 (2022).
- ¹¹⁶B. Kulkarni, and M. Jayakannan, ACS Biomater. Sci. Eng. 3, 2185 (2017).
- ¹¹⁷W. Zhang, F. Huo, F. Cheng, and C. Yin, JACS. **142**, 6324 (2020).
- ¹¹⁸D. Bahari, B. Babamiri, A. Salimi, and A. Rashidi, J. Lumin. **239**, 118371 (2021).
- ¹¹⁹P. Ashokkumar, N. Adarsh, and A.S. Klymchenko, Small. **16**, 2002494 (2020).
- ¹²⁰H. Dong, L.D. Sun, W. Feng, Y. Gu, F. Li, and C.H. Yan, ACS Nano 11, 3289 (2017).
- ¹²¹C. Liu, Z. Gao, J. Zeng, Y. Hou, F. Fang, Y. Li, R. Qiao, L. Shen, H. Lei, W. Yang, and M. Gao, ACS Nano 7, 7227 (2013).
- ¹²²Q. Liu, W. Feng, T. Yang, T. Yi, and F. Li, Nat. Protoc. **8**, 2033 (2013).
- ¹²³ M. Yu. F. Li, Z. Chen, H. Hu, C. Zhan, H. Yang, and C. Huang, Anal. Chem. 81, 930 (2009).
- ¹²⁴L. Xiong, Z. Chen, Q. Tian, T. Cao, C. Xu, and F. Li, Anal. Chem. **81**, 8687 (2009).
- ¹²⁵B.B. Ding, H.Y. Peng, H.S. Qian, L. Zheng, and S.H. Yu, Adv. Mater. Interfaces. 3, 1500649 (2016).
- ¹²⁶ X. Li, L. Liu, Y. Fu, H. Chen, M.M. Abualrejal, H. Zhang, Z. Wang, and H. Zhang, Acta. Biomater. **104**, 167 (2020).
- ¹²⁷O.S. Kwon, H.S. Song, J. Conde, H.I. Kim, N. Artzi, and J.H. Kim, ACS Nano, **10**, 1512.
- ¹²⁸ C. Li, Z. Hou, Y. Dai, D. Yang, Z. Cheng, and J. Lin, Biomater. Sci. 1, 213 (2013).
- ¹²⁹ A. Gulzar, J. Xu, D. Yang, L. Xu, F. He, S. Gai, and P. Yang, Dalton. Trans. 47, 3931 (2018).
- ¹³⁰A. Zamora-Gálvez, E. Morales-Narváez, C.C. Mayorga-Martinez, and A. Merkoçi, Appl Mater Today. 9, 7756 (2017).
- ¹³¹J.N. Tiwari, V. Vij, K.C. Kemp, and K.S. Kim, ACS Nano. **10**, 46 (2016).
- ¹³²M. Ebara, Biomaterials Nanoarchitectonics 1 (2016).
- ¹³³J.S. Wilson, Sensor Technology Handbook 1 (2005).
- ¹³⁴P.F. Pinsky, P.C. Prorok, and B.S. Kramer, New England Journal of Medicine **376**, 1285 (2017).
- ¹³⁵H. Afsharan, F. Navaeipour, B. Khalilzadeh, H. Tajalli, M. Mollabashi, M.J. Ahar, and M.R. Rashidi, Biosens Bioelectron **80**, 146 (2016).

- ¹³⁶J. Zhao, Y. Tang, Y. Cao, T. Chen, X. Chen, X. Mao, Y. Yin, and G. Chen, Electrochim Acta 283, 1072 (2018).
- ¹³⁷S. Ferdinandusse, S. Denis, L. Ijlst, G. Dacremont, H.R. Waterham, and R.J.A. Wanders, J Lipid Res **41**, 1890 (2000).
- ¹³⁸K.S. Prasad, X. Cao, N. Gao, Q. Jin, S.T. Sanjay, G. Henao-Pabon, and X.J. Li, Sens Actuators B Chem **305**, 127516 (2020).
- ¹³⁹D. Tang, R. Yuan, and Y. Chai, Clin Chem **53**, 1323 (2007).
- ¹⁴⁰S. Kadian, A. Kalkal, V. Jain, S. Shukla, and R.J. Narayan, MRS Comm. 1 (2023)
- ¹⁴¹S.A. Machekposhti, S. Kadian, L. Vanderwal, S. Stafslien, and R.J. Narayan, MedComm. 4, (2023)
- ¹⁴²S. Kadian, N. Chaulagain, N.N. Joshi, K.M. Alam, K. Cui, K. Shankar, G. Manik, and R.J. Narayan, Nanotechnol. **34**, 30LT01 (2023).
- ¹⁴³ T.M. Lwin, M.A. Turner, S. Amirfakhri, H. Nishino, P. Debie, B.C. Cosman, R.M. Hoffman, S. Hernot, and M. Bouvet, J. Surg. Oncol. 124, 1121 (2021).
- ¹⁴⁴A. Russegger, A.C. Debruyne, D.C. Berrio, S. Fuchs, J. Marzi, K. Schenke-Layland, R.I. Dmitriev, and S.M. Borisov, Adv. Opt. Mater. 2202720 (2023).
- ¹⁴⁵I.A. Okkelman, R. McGarrigle, S. O'Carroll, D.C. Berrio, K. Schenke-Layland, J. Hynes, and R.I. Dmitriev, ACS Appl. Biomater. **3**, 5310 (2020).
- ¹⁴⁶X. Li, C. Shen, M. Yang, and A. Rasooly, Anal Chem **90**, 4764 (2018).
- ¹⁴⁷A. Chen, W. Liang, H. Wang, Y. Zhuo, Y. Chai, and R. Yuan, Anal Chem **92**, 1379 (2020).
- ¹⁴⁸S. Kasturi, Y. Eom, S.R. Torati, and C.G. Kim, Journal of Industrial and Engineering Chemistry 93, 186 (2021).
- ¹⁴⁹A. Bharti, S. Mittal, S. Rana, D. Dahiya, N. Agnihotri, and N. Prabhakar, Anal Biochem **609**, 113908 (2020).
- ¹⁵⁰J.M. Moon, Y. Hui Kim, and Y. Cho, Biosens Bioelectron **57**, 157 (2014).
- ¹⁵¹C. Pothipor, S. Bamrungsap, J. Jakmunee, and K. Ounnunkad, Colloids Surf B Biointerfaces 210, 112260 (2022).
- ¹⁵²J. Tian, J. Huang, Y. Zhao, and S. Zhao, Microchimica Acta 178, 81 (2012).
- ¹⁵³B. Kavosi, A. Salimi, R. Hallaj, and F. Moradi, Biosens Bioelectron **74**, 915 (2015). ¹⁵⁴Q. Wu, Z. Li, Q. Liang, R. Ye, S. Guo, X. Zeng, J. Hu, and A. Li, Electrochim Acta **428**, 140945 (2022).
- ¹⁵⁵M. Azimzadeh, M. Rahaie, N. Nasirizadeh, K. Ashtari, and H. Naderi-Manesh, Biosens Bioelectron 77, 99 (2016).
- ¹⁵⁶Q. Ma, J Electrochem Soc **168**, 027515 (2021).
- ¹⁵⁷R. Salahandish, A. Ghaffarinejad, E. Omidinia, H. Zargartalebi, K. Majidzadeh-A, S.M. Naghib, and A. Sanati-Nezhad, Biosens Bioelectron **120**, 129 (2018).
- ¹⁵⁸Y. Luo, Y. Wang, H. Yan, Y. Wu, C. Zhu, D. Du, and Y. Lin, Anal Chim Acta **1042**, 44 (2018).
- ¹⁵⁹A. Roberts, P.P. Tripathi, and S. Gandhi, Biosens Bioelectron 141, 111398 (2019).

- ¹⁶⁰J. Okuno, K. Maehashi, K. Kerman, Y. Takamura, K. Matsumoto, and E. Tamiya, Biosens Bioelectron 22, 2377 (2007). ¹⁶¹S.
- Kumar, J.G. Sharma, S. Maji, and B.D. Malhotra, Biosens Bioelectron **78**, 497 (2016). ¹⁶²M. Pal and R. Khan, Anal Biochem **536**, 51 (2017).
- ¹⁶³Deepa, B. Nohwal, and C.S. Pundir, Microchemical Journal **156**, 104957 (2020).
- ¹⁶⁴U. Rajaji, A. Muthumariyappan, S.M. Chen, T.W. Chen, and R.J. Ramalingam, Sens Actuators B Chem 291, 120 (2019).
- ¹⁶⁵S. Rauf, G.K. Mishra, J. Azhar, R.K. Mishra, K.Y. Goud, M.A.H. Nawaz, J.L. Marty, and A. Hayat, Anal Biochem 545, 13 (2018).
- ¹⁶⁶S. Kadian, S.K. Sethi, and G. Manik, Mater Chem Front 5, 627 (2021).
- ¹⁶⁷S. Kadian, G. Manik, N. Das, P. Nehra, R.P. Chauhan, and P. Roy, J Mater Chem B 8, 3028 (2020).
- ¹⁶⁸A. Kalkal, R. Pradhan, S. Kadian, G. Manik, and G. Packirisamy, ACS Appl Bio Mater **3**, 4922 (2020). ¹⁶⁹S. Kadian and G. Manik, Luminescence **35**, 763 (2020).
- ¹⁷⁰D.L. Li, J.E. Tan, Y. Tian, S. Huang, P.H. Sun, M. Wang, Y.J. Han, H.S. Li, H.B. Wu, X.M. Zhang, Y.K. Xu, and Q.S. Wang, Biomaterials **147**, 86 (2017).
- ¹⁷¹A. Kalkal, S. Kadian, R. Pradhan, G. Manik, and G. Packirisamy, Mater Adv 2, 5513 (2021).
- ¹⁷²W. Cao, W. Gao, Z. Liu, W. Hao, X. Li, Y. Sun, L. Tong, and B. Tang, Anal Chem **90**, 9125 (2018).
- ¹⁷³Y. Wen, V.X. Truong, and M. Li, Nano Lett **21**, 3066 (2021).
- ¹⁷⁴P.D. Nguyen, V.T. Cong, C. Baek, and J. Min, Biosens Bioelectron **89**, 666 (2017).
- ¹⁷⁵J. Shi, J. Lyu, F. Tian, and M. Yang, Biosens Bioelectron **93**, 182 (2017).
- ¹⁷⁶P. Suriamoorthy, X. Zhang, G. Hao, A.G. Joly, S. Singh, M. Hossu, X. Sun, and W. Chen, Cancer Nanotechnol 1, 19 (2010).
- ¹⁷⁷N.Y. Morgan, S. English, W. Chen, V. Chernomordik, A. Russo, P.D. Smith, and A. Gandjbakhche, Acad Radiol 12, 313 (2005).
- ¹⁷⁸S. Kadian, G. Manik, N. Das, and P. Roy, Microchimica Acta **187**, 1 (2020).
- ¹⁷⁹S. Wu, M. Wei, H. Yang, J. Fan, W. Wei, Y. Zhang, and S. Liu, Sens Actuators B Chem **259**, 565 (2018).
- ¹⁸⁰Q. Wu, N. Li, Y. Wang, Y. liu, Y. Xu, S. Wei, J. Wu, G. Jia, X. Fang, F. Chen, and X. Cui, Biosens Bioelectron **144**, 111697 (2019).
- ¹⁸¹X. Hao, C. Li, Y. Zhang, H. Wang, G. Chen, M. Wang, and Q. Wang, Advanced Materials 30, 1804437 (2018).
- ¹⁸²Y. Han, J. Chen, Z. Li, H. Chen, and H. Qiu, Biosens Bioelectron **148**, 111811 (2020).
- ¹⁸³S. Kadian, G. Manik, A. Kalkal, M. Singh, and R.P. Chauhan, Nanotechnology 30, 435704 (2019).
- ¹⁸⁴S. Şahin, M.O. Caglayan, and Z. Üstündağ, Microchimica Acta **187**, 1 (2020).
- ¹⁸⁵A. Kalkal, S. Kadian, R. Pradhan, G. Manik, and G. Packirisamy, Mater Adv 2, 5513 (2021).
- ¹⁸⁶Y. Xia, L. Wang, J. Li, X. Chen, J. Lan, A. Yan, Y. Lei, S. Yang, H. Yang, and J. Chen, Anal Chem **90**, 8969 (2018).
- ¹⁸⁷N. Li, R. Li, Z. Li, Y. Yang, G. Wang, and Z. Gu, Sens Actuators B Chem **283**, 666 (2019).

- ¹⁸⁸I. al Ogaidi, H. Gou, Z.P. Aguilar, S. Guo, A.K. Melconian, A.K.A. Al-Kazaz, F. Meng, and N. Wu, Chemical Communications **50**, 1344 (2014).
- ¹⁸⁹G. min Ma, L. wei Huo, Y. xia Tong, Y. cong Wang, C. ping Li, and H. xia Jia, Microchimica Acta 188, 1 (2021).
- ¹⁹⁰Y.S. Borghei, M. Hosseini, and M.R. Ganjali, Microchimica Acta 184, 2671 (2017).
- ¹⁹¹Y. Zhang, S. Guo, H. Huang, G. Mao, X. Ji, and Z. He, Anal Chim Acta **1035**, 154 (2018).
- ¹⁹²T.M. Lwin, M.A. Turner, H. Nishino, S. Amirfakhri, S. Hernot, R.M. Hoffman and M. Bouvet, Biomolecules. 12, 711 (2022).
- ¹⁹³L. Mateusiak, S. Floru, J. Wouters, T. De Groof, N. Declerck, S. Janssen, P. Debie, K. Zeven, J. Puttemans, K. Breckpot, and N.
- Devoogdt, (2023)¹⁹⁴A. Azzouz, L. Hejji, K.H. Kim, D. Kukkar, B. Souhail, N. Bhardwaj, R.J.C. Brown, and W. Zhang, Biosens Bioelectron **197**, 113767 (2022).
- ¹⁹⁵Q. Wang, L. Zou, X. Yang, X. Liu, W. Nie, Y. Zheng, Q. Cheng, and K. Wang, Biosens Bioelectron 135, 129 (2019).
- ¹⁹⁶K. Zhang, F. Lu, Z. Cai, S. Song, L. Jiang, Q. Min, X. Wu, and J.J. Zhu, Anal Chem **92**, 11795 (2020).
- ¹⁹⁷Z. Fattahi, A.Y. Khosroushahi, and M. Hasanzadeh, Biomedicine and Pharmacotherapy **132**, 110850 (2020).
- ¹⁹⁸M. Loyez, M. Lobry, E.M. Hassan, M.C. DeRosa, C. Caucheteur, and R. Wattiez, Talanta **221**, 121452 (2021).
- ¹⁹⁹M. Jia, S. Li, L. Zang, X. Lu, and H. Zhang, Nanomaterials **8**, 730 (2018).
- ²⁰⁰K. Xu, R. Zhou, K. Takei, and M. Hong, Advanced Science **6**, 1900925 (2019).
- ²⁰¹K.H. Huynh, E. Hahm, M.S. Noh, J.H. Lee, X.H. Pham, S.H. Lee, J. Kim, W.Y. Rho, H. Chang, D.M. Kim, A. Baek, D.E. Kim, D.H. Jeong, S.M. Park, and B.H. Jun, Nanomaterials **11**, 1215 (2021).
- ²⁰²S.J. Lee, H. Lee, T. Begildayeva, Y. Yu, J. Theerthagiri, Y. Kim, Y.W. Lee, S.W. Han, and M.Y. Choi, Biosens Bioelectron **197**, 113766 (2022).
- ²⁰³A. Alyami, A.J. Quinn, and D. Iacopino, Talanta **201**, 58 (2019).
- ²⁰⁴Y. Hou, W. Zhang, S. Li, Z. Wang, H. Zhong, Z. Liu, and Z. Guo, Analyst **143**, 3677 (2018).
- ²⁰⁵Z. Zhang, J. Wang, K.B. Shanmugasundaram, B. Yeo, A. Möller, A. Wuethrich, L.L. Lin, and M. Trau, Small 16, 1905614 (2020).
- ²⁰⁶J. Wang, D. Liang, J. Feng, and X. Tang, Anal Chem **91**, 11045 (2019).
- ²⁰⁷S. Meng, R. Chen, J. Xie, J. Li, J. Cheng, Y. Xu, H. Cao, X. Wu, Q. Zhang, and H. Wang, Biosens Bioelectron **190**, 113470 (2021).
- ²⁰⁸J. Wang, K.M. Koo, E.J.H. Wee, Y. Wang, and M. Trau, Nanoscale **9**, 3496 (2017).
- ²⁰⁹O. Li, X. Ge, J. Ye, Z. Li, L. Su, Y. Wu, H. Yang, and J. Song, Angewandte Chemie International Edition **60**, 7323 (2021).
- ²¹⁰ S. Song, Y. Wang, Y. Zhao, W. Huang, F. Zhang, S. Zhu, Q. Wu, S. Fu, B.Z. Tang, and D. Wang, Matter. 5, 2847 (2022).
- ²¹¹Z. Fang, D., Chen, J. Xu, J. Wang, S. Li, X. Tian, Y. Tian, and O. Zhang, Anal. Chem. **94**, 14769 (2022).
- ²¹²C.Y.S. Chung, J.M. Posimo, S. Lee, T. Tsang, J.M. Davis, D.C. Brady, and C.J. Chang, 2019. PNAS. **116**, 18285 (2019).

²¹³ E.J. Ge, A.I. Bush, A. Casini, P.A. Cobine, J.R. Cross, G.M. DeNicola, Q.P. Dou, K.J. Franz, V.M. Gohil, S. Gupta, and S.G. Kaler, Nat. Rev. Cancer. **22**, 102 (2022).

²¹⁴ B. Tan, C. Zhao, J. Wang, A. Tiemuer, Y. Zhang, H. Yu, and Y. Liu, Acta Biomaterialia. 155, 554 (2023).

²¹⁵S. Shukla, J. Jakowski, S. Kadian, and R.J. Narayan, Comput. Struct. Biotechnol. J. **21**, 4149 (2023)

Figure Captions

Fig. 1. A) AIE luminogens. (1) Chemical structure of hexaphenylsilole HPS, (2) HPS solutions in acetonitrile–water mixtures containing different volume fractions of water; pictures taken on exposure to UV lamp, (3) heteroatom containing fluorophores with corresponding colors displayed in visible region on emission; derivatives of stilbene (1), silole (2, 5 and 6), tetraphenyl ethylene, TPE (3, 4), di fluoro boron complex of triphenyl amine, BF₂ – TPA (7).³⁰ A) Reproduced with permission from Hong et al., *Chem. Commun.* **29**, 332 (2009) Copyright 2009 Royal Society of Chemistry. B). (1) Targeted assembly of AIE luminogen **TIFMN**, with acceptor, donor conjugated together with a p bridge, (2) confocal images of 786-O cells a) before and after the laser irradiation for b) 1 min, c) 3 min, and d) 5 min stained with **TIFMN** (5 μM).⁴² B) Reproduced with permission from Tan et al., Dyes Pigm. **188**, 109215 (2021). Copyright 2021 Elsevier. C) (1) Induction of aggregation in mangiferin, (2) Confocal images of cancer cells and their corresponding normal cells were carried out (HeLa (a1-a3) and H8 (e1-e3), SW480 (b1-b3) and NCM460 (f1-f3), MCF-7 (c1-c3) and MCF-10A (g1-g3), SKOV-3 (d1-d3) and IOSE80 (h1-h3)) on incubation with mangiferin (100 μg mL⁻¹, 1 mL) for 3 h on bright channel (a1-h1), red channel (a2-h2) and merged (a3-h3).⁴³ C) Reproduced with permission from Long et al., Sens. Actuators. Chem. **348**, 130666 (2021). Copyright 2009 Elsevier.

Fig. 2. (A – B) Energy level diagram for PET mechanism, (A) a – PET, (B) d – PET. ¹⁰⁷ (A – B) Reproduced with permission from Sun et al., Acc. Chem. Res. 52, 2818 (2019). Copyright 2019 American Chemical Society. (C) Schematic illustration of fluorescence 'turn on' mechanism allowing for the concurrent detection of low pH and Zn²⁺ Grey – weak fluorescence emission intensity. Green – strong fluorescence emission intensity. ¹⁰⁸ (C) Reproduced with permission from Du et al., Chem. Sci. 10, 5699 (2019). Copyright 2019 Royal Society of Chemistry. (D) Chemical structure and sensing mechanism of NB-AX to KIAA1363. ¹⁰⁷ (D) Reproduced with permission from Sun et al., Acc. Chem. Res. 52, 2818 (2019). Copyright 2019 American Chemical Society. (E) Confocal fluorescence images of A549 cells incubated with (1) PEI-Cu NCs, and (2) PEI-Cu NCs + PNPP. ¹⁰⁶ (E) Reproduced with permission from Huang et al., Anal. Chim. Acta. 1142, 65 (2021). Copyright 2021 Elsivier. (F) Fluorescence microscopic images of prostate cancer cells, PC3 and DU145,

and normal human prostate epithelial cells, RWPE1, incubated with LysoDPP-C4 (1 mM, 24 h) in the absence and presence of an exogenous zinc source (15 mM – ZnSO₄). (F) Reproduced with permission from Du et al., Chem. Sci. 10, 5699 (2019) Copyright 2019 Royal Society of Chemistry. (G) The synthetic route of ADC-IMC-2 and ADC-IMC-6. (G) Reproduced with permission from Chen et al., SAA. 241, 118685 (2020). Copyright 2020 Elsevier. (H) UV – Visible absorption spectra of the assistant test to verify the hyperchromic effect of PNP, all the concentration of PEI-Cu NCs, PNPP, PNP, and ALP are 50 mL, 10 mM, 1 mM, and 50 U/L, respectively. Experimental condition: pH (8.0), reaction time (40 min), the concentration of PNPP (10 mM), temperature (37 °C). (H) Reproduced with permission from Huang et al., Anal. Chim. Acta. 1142, 65 (2021). Copyright 2021 Elsevier.

Fig. 3. (A) Change from FRET to no FRET condition on Enzymatic biodegradation of PCL segments in the block copolymers. (B) Confocal images of the P30 polymer, NR encapsulated control polymer (polymer + NR), and P30-NR polymer (a) incubated with HeLa cells. ¹¹⁶ (A – B) Reproduced with permission from Kulkarni and Jayakannan et al., ACS Biomater. Sci. Eng. 3, 2185 (2017). Copyright 2017 American Chemical Society. (C) Synergistic FRET and ICT process for GSH and SO₂ sensing, with (i) donor, (ii) acceptor centers. ¹¹⁷ (C) Reproduced with permission from Zhang et al., JACS. 142, 6324 (2020). Copyright 2020 American Chemical Society. (D) Fluorescence lifetime decay spectra of GDQD + GQD. (E) fluorescence microscopy images of MDA-MB 231 cells incubated with GDQD-microRNA-21 under the excitation of 405 nm for all images, the scale bar is 25 μm. ¹¹⁸ (D – E) Reproduced with permission from Bahari et al., J. Lumin. 239, 118371 (2021). Copyright 2021 Elsevier.

Fig. 4. Schematic illustration showing Proposed energy transfer mechanism under 980 and 808 nm continuous wave (CW) laser excitation in nano dumbbells. Reproduced with permission from Ding *et al.*, Adv. Mater. Interfaces. **3**, 1500649 (2016). Copyright 2016 John Wiley and Sons.

Fig. 5. (A) Schematic illustration showing modification of UCNPs with tumor targeting peptides for UCL/MR dual mode bioimaging. (B) *In vivo* UCL images of HCT116 tumor-bearing BALB/c nude mice with intravenous injection of 10 mg kg-1 (Gd content) (a) UCNP@SiO₂-COOH, (b) UCNP@SiO₂-l-SP5-H and (c) UCNP@SiO₂-l-SP5-C at various time points (0, 1, 2, 4, 6, 8, 24 and 48 h, the 0 h means pre-injection) of post-injection, respectively. (A – B) Reproduced with permission from Li *et al.*, Acta. Biomater. **104**, 167 (2020). Copyright 2020 Elsevier.

Fig. 6. (A) Schematic illustration for the synthesis of UCNPs@mSiO₂-PEG/FAcomposite nanospheres. (B) Confocal laser scanning microscopy (CLSM) of HeLa cells incubated with DOX-UCNPs@mSiO₂-PEG/FA (a–c), DOX-UCNPs@mSiO₂-PEG (d–f) and DOX-UCNPs@mSiO₂-PEG/FA (a–c), DOX-UCNPs@mSiO₂-PEG (d–f) and DOX-UCNPs@mSiO₂-PEG/FA (a–c), DOX-UCNPs@mSiO₂-PEG (d–f) and DOX-UCNPs@mSiO₂-PEG/FA (a–c), DOX-UCNPs@mSiO

UCNPs @mSiO₂-PEG/FA + free FA (g–i) for 1 h at 37 °C. ¹²⁸ (A – B) Reproduced with permission from Li *et al.*, Biomater. Sci. **1**, 213 (2013). Copyright 2013 Royal Society of Chemistry.

Fig. 7 Nanomaterials based electrochemical probes. (A) Schematic representation of (i) synthesis process of Au/Ag NRs-Ab2 and (ii) step wise design and development of the dual-mode electrochemical immunosensor ¹⁵⁶. Reproduced with permission from Ma, *J. Electrochem. Soc. 168, 027515 (2021)*. (B) Schematic diagram of stepwise fabrication of nanocomposite; 1) Deposition of N-doped functionalized graphene (NFG) onto FTO electrode; 2) Electrodeposition of AgNPs; 3) Electropolymerization of PANI onto NFG/Ag substrate; 4) Carboxylic group functionalization via 1-Ethyl-3-(3 dimethylaminopropyl) carbodiimide hydrochloride (EDC)/N-hydroxy succinimide (NHS) chemistry; 5) Adsorption of ss-DNA probe; 6) Addition of 11-mercapto-1-undecanol (MU) for blocking all unused sites and orienting the bonded miRNA-21; 7) Electrochemical sensing of miRNA-21; 8) Assessment of sensing process using differential pulse voltammetry (DPV) ¹⁵⁷. Reproduced with permission from Salahandish *et al.*, Biosens Bioelectron 120, 129 (2018). Copyright 2018 Elsevier. (C) Schematic diagram of fabrication of dual-signal amplification non-enzymatic electrochemical sensing platform using single-walled CNTs@ GQDs nanocomposite ¹⁵⁸. Reproduced with permission from Luo *et al.*, Anal Chim Acta 1042, 44 (2018). Copyright 2018 Elsevier.

Fig. 8. (A) Schematic illustration of mechanism of amine functionalized and nitrogen-doped GQDs (amine-N-GQDs) based fluorescent biosensor for small cell lung cancer biomarker detection ¹⁶⁸. Reproduced with permission from Kalkal *et al.*, ACS Appl Bio Mater 3, 4922 (2020). Copyright 2020 American Chemical Society. (B) Schematic diagram of design and synthesis process of PEHA-GQD-His optical probe for the detection of miRNA through molecular beacon double cycle amplification strategy ¹⁸⁷. Reproduced with permission from Nana *et al.*, Sens Actuators B Chem 283, 666 (2019). Copyright 2019 Elsevier.

Fig. 9 (A) Schematic illustration of Dual AuNP-assisted signal amplification strategy for the development of aptamer-based SPR sensor for sensitive detection of exosomes¹⁹⁵. Reproduced with permission from Wang *et al.*, Biosens Bioelectron 135, 129 (2019). Copyright 2019 Elsevier. (B) Schematic representation of (a) enhancement in the luminescence intensity of the green-fluorescent AuNRs@SiO2-UCNPs nanocomposite and (b, c) design of the AuNRs SPR effect-based sensing platform for the sensitive detection of miRNAs ¹⁹⁶. Reproduced with permission from Zhang *et al.*, Anal Chem 92, 11795 (2020). Copyright 2020 American Chemical Society.

Fig. 10. (A) Schematic illustration of development of label-free optical SERS sensing probe using the total RNA extracted from urine and amplification strategy to directly detect multiple RNA biomarkers ²⁰⁸. Reproduced with permission from Wang *et al.*, Nanoscale 9, 3496 (2017). Copyright 2017 Royal Society of Chemistry. (B) Schematic diagram of the dual ratiometric SERS signals generating

core-satellite nanostructure for the detection of oxidative species produced during inflammation and cancer. In the presence of oxidative species, the external AuNPs of nanostructure dissociate, which weakens the intensity of the SERS peak while the intensity of SERS peak corresponding to nanogapped AuNR does not change, forming the oxidative species-responsive ratiometric SERS sensing platform ²⁰⁹. Reproduced with permission from Li *et al.*, Angewandte Chemie - International Edition 60, 7323 (2021). Copyright 2020 Wiley Online Library.

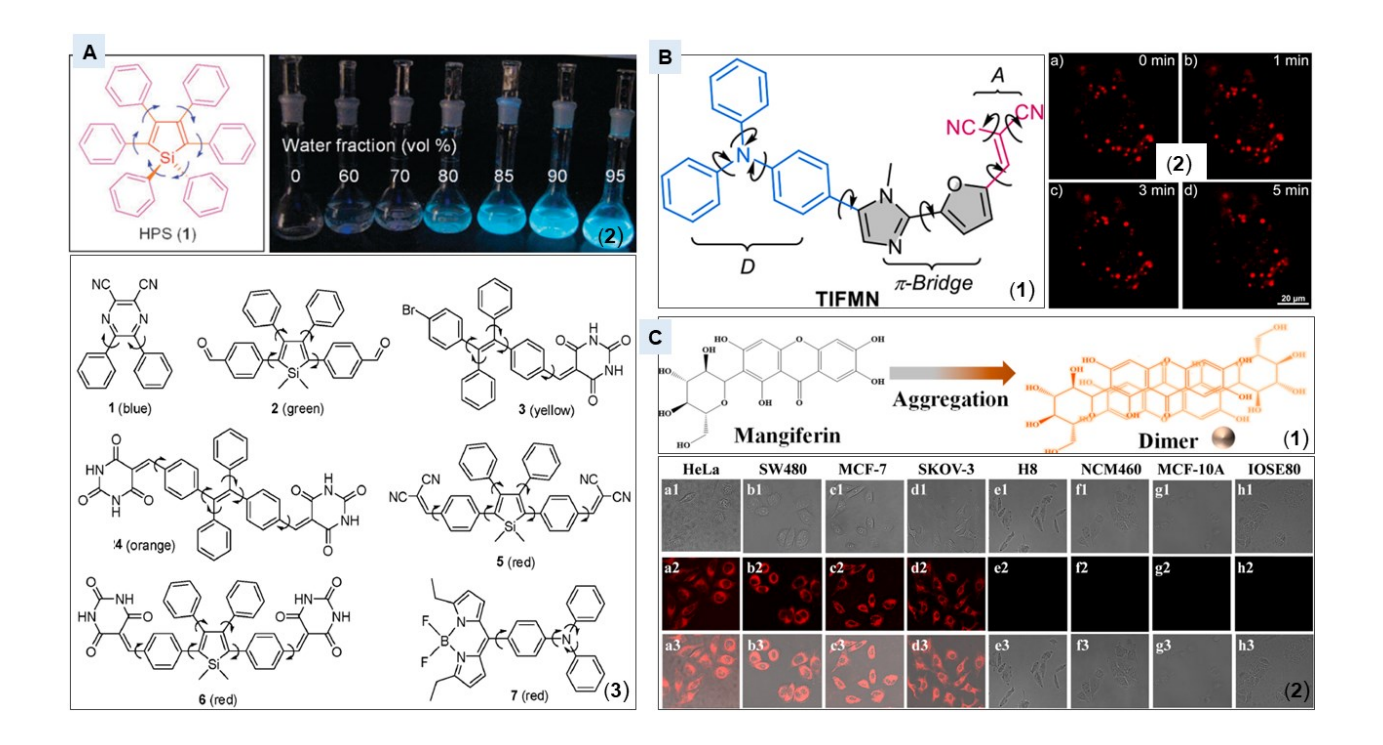


Figure 1

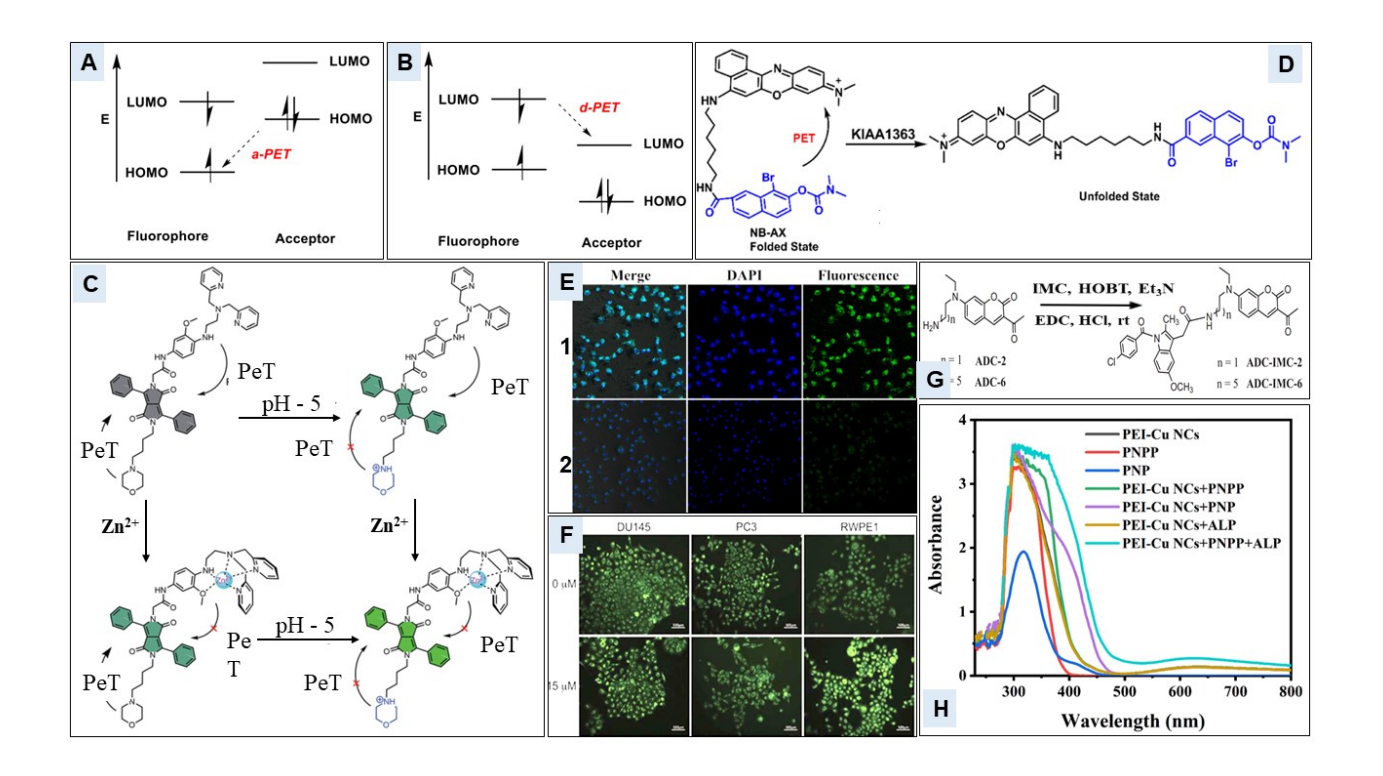


Figure 2

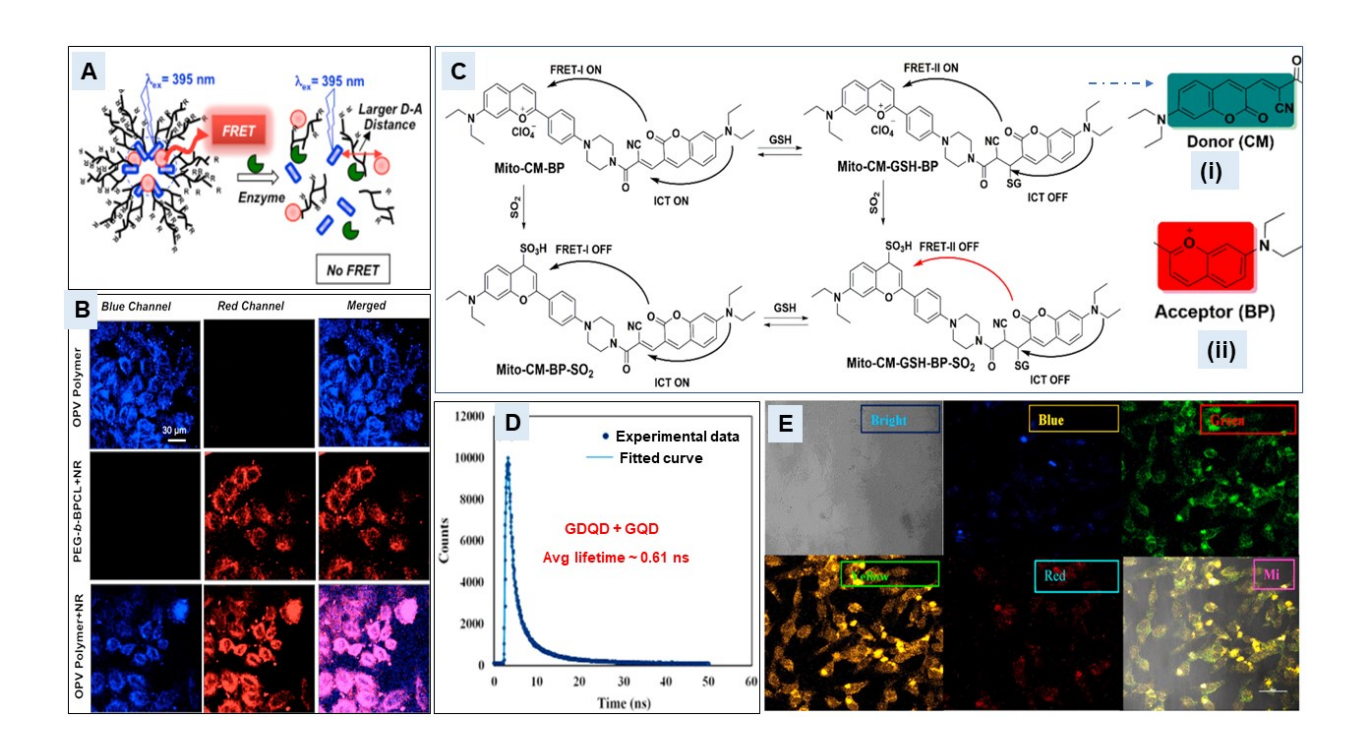


Figure 3

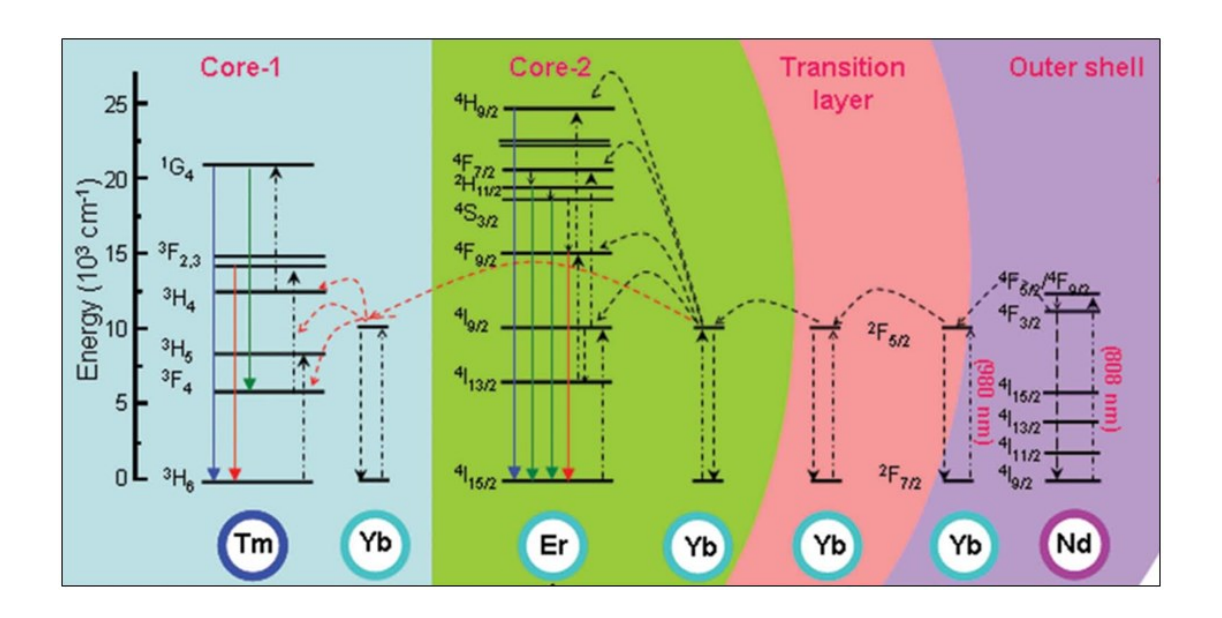


Figure 4

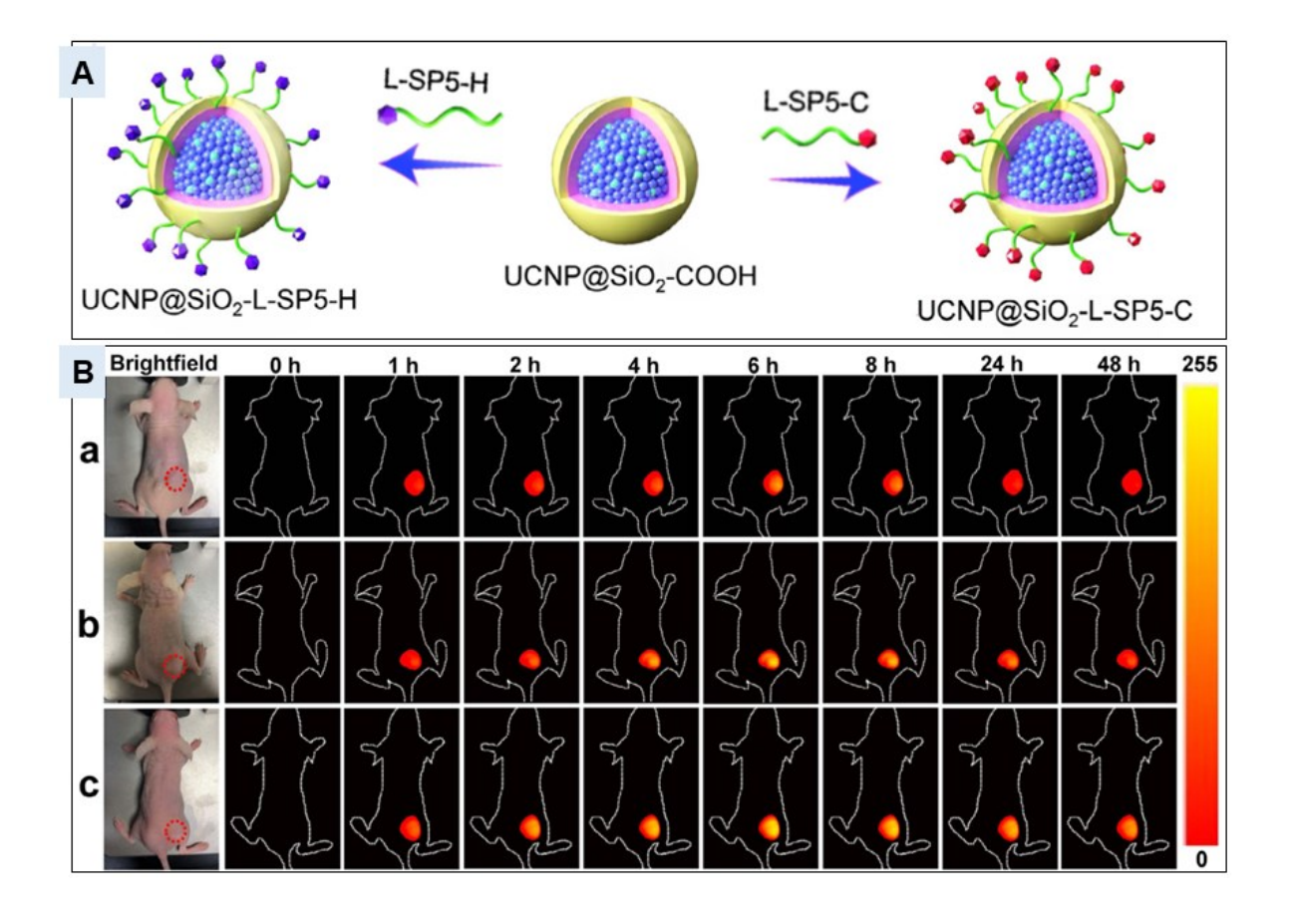


Figure 5

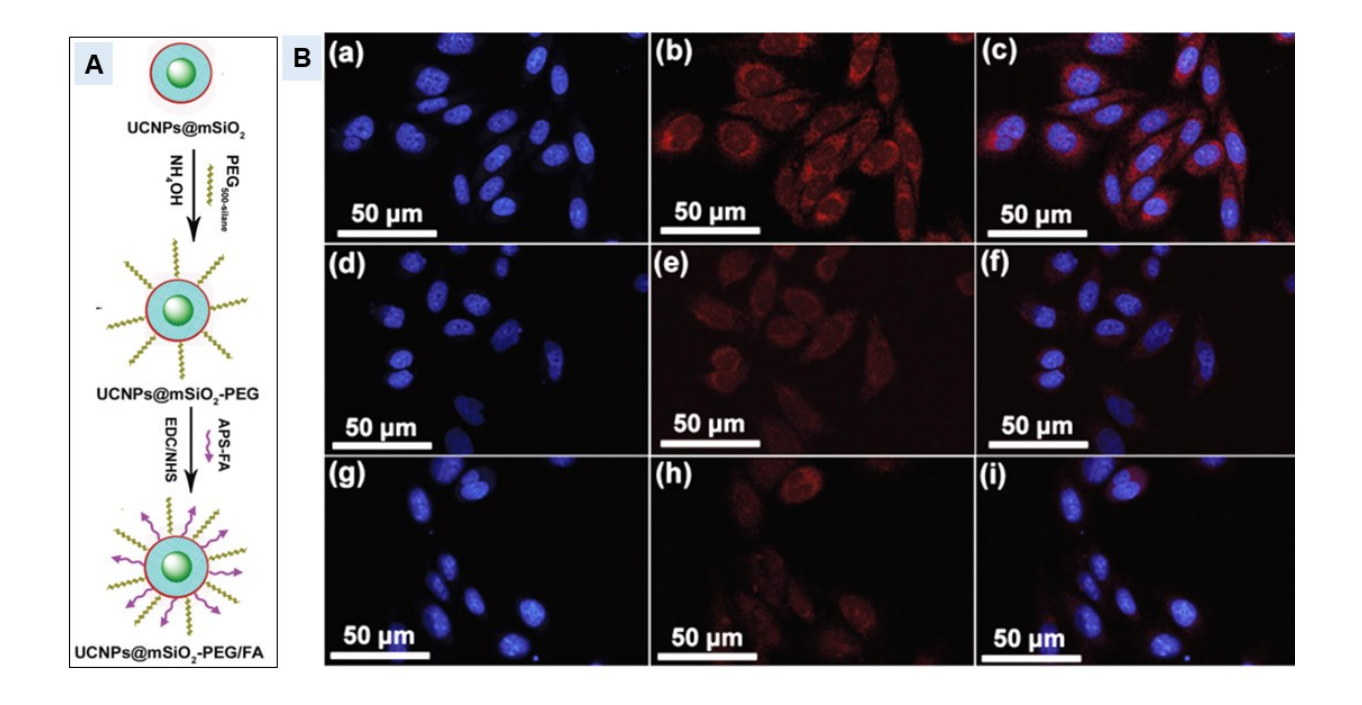


Figure 6

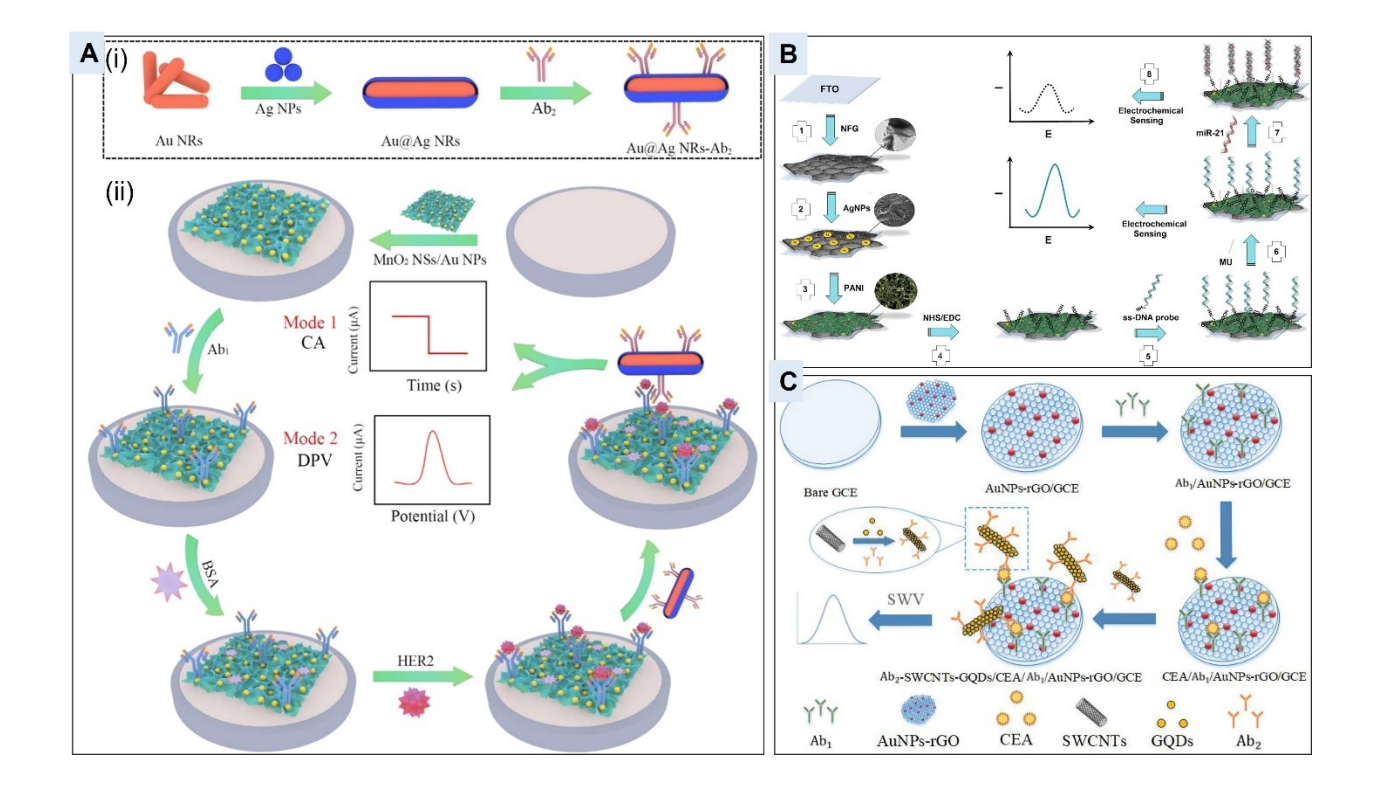


Figure 7

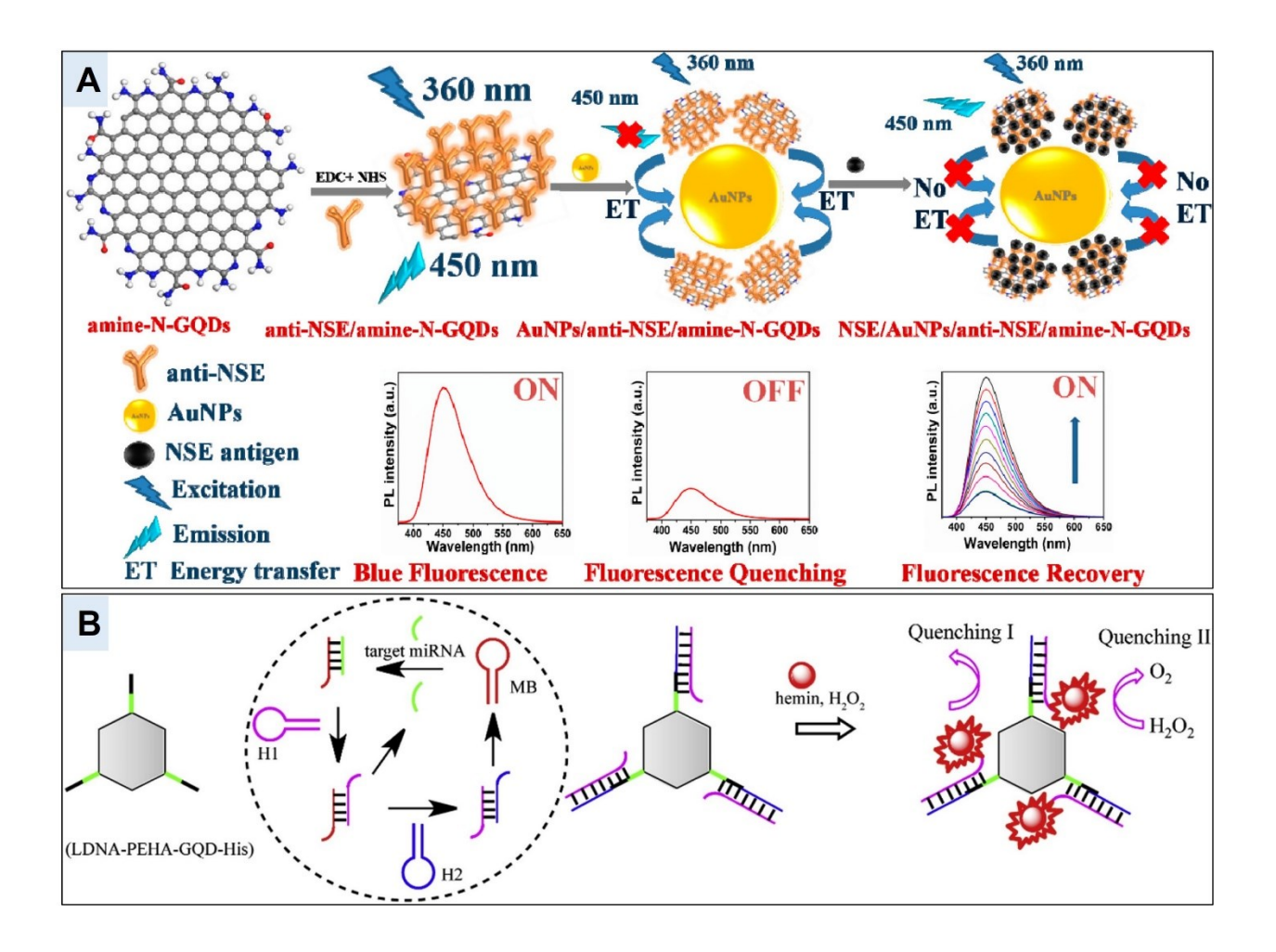


Figure 8

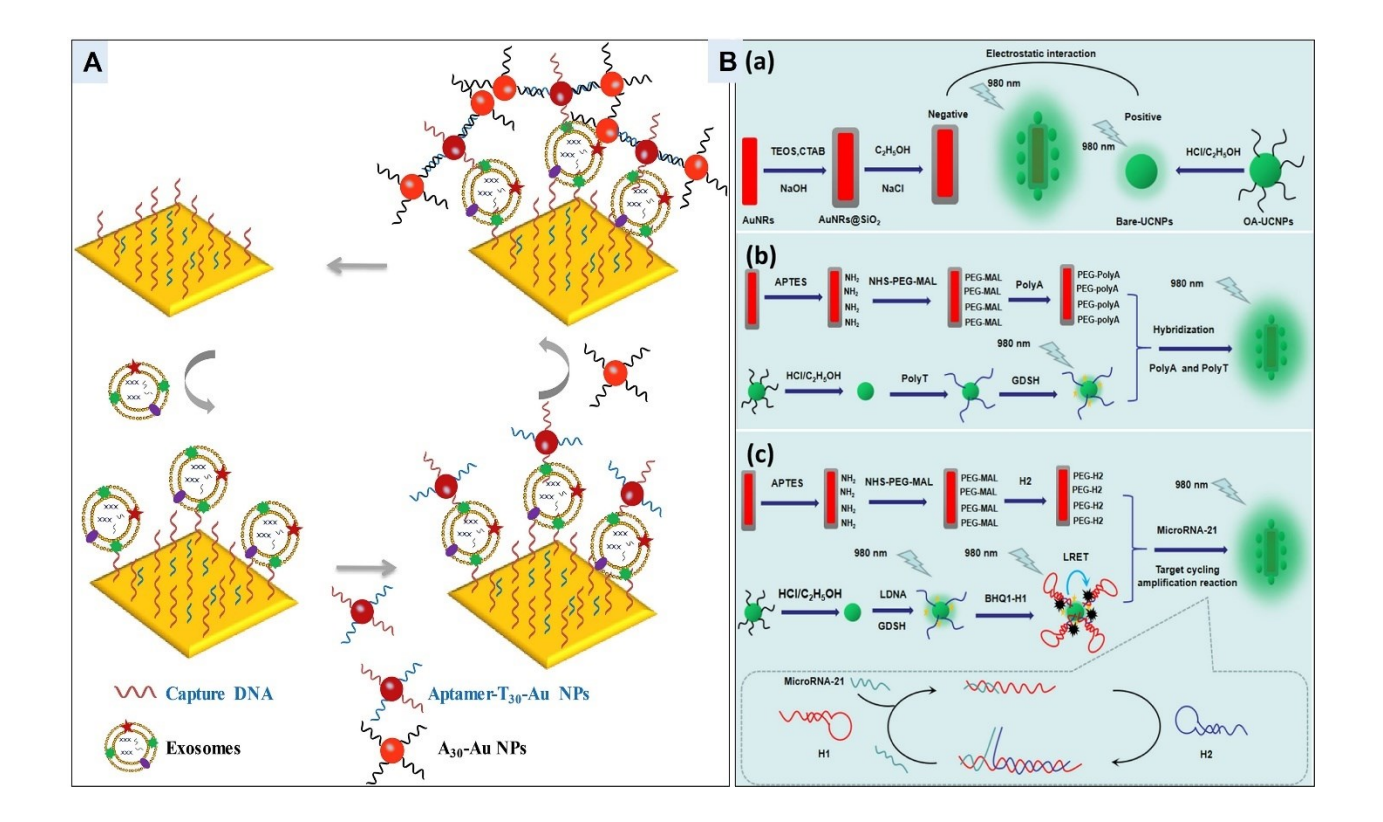


Figure 9

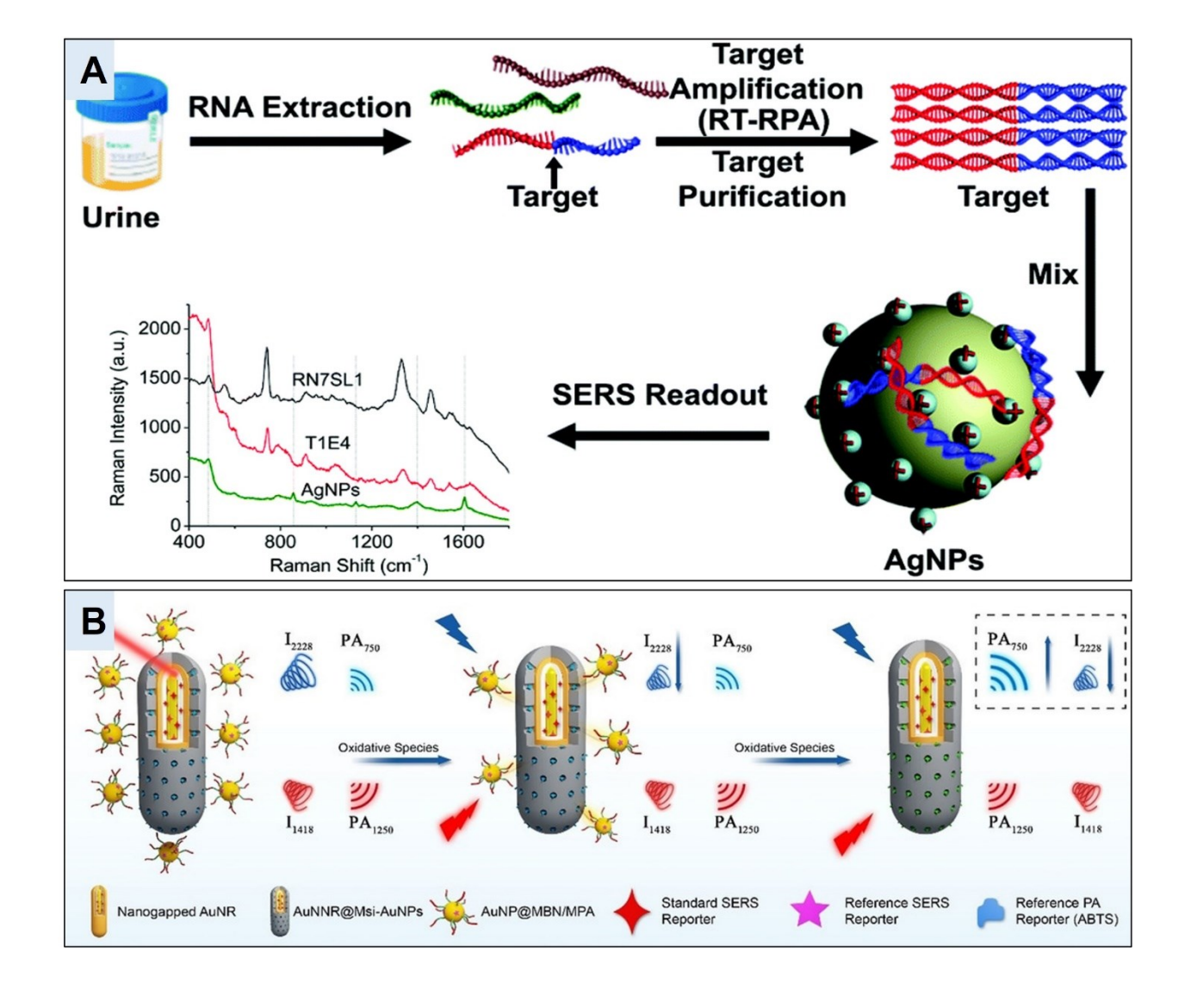


Figure 10